Water Balance and Slope Stability in a Changing Climate: Combinatorial Influences of Rainfall and Snowmelt Induced Himalayan Geohazards

Deepali Anand[1], Arindam Dey[1*] and Ravi K.[1]

Deepali Anand
Research Scholar, Department of Civil Engineering, Indian Institute of Technology Guwahati, Assam, India. ORCID No.: 0000-0002-0072-2236 Email: a.deepali@iitg.ac.in

Arindam Dey*
Associate Professor, Department of Civil Engineering and the Center for Disaster Management and Research (CDMR), Indian Institute of Technology Guwahati, Assam, India. ORCID No.:0000-0001-7007-2729 Contact No.: +918011002709 Email: arindamdeyiitg16@gmail.com
* Corresponding author

Ravi K.
Associate Professor, Department of Civil Engineering, Indian Institute of Technology Guwahati, Assam, India. Email: ravi.civil@iitg.ac.in

Funding and Acknowledgment: This study belongs to a part of the project 'Study of Glacial Dynamics and Sustainable Hydrological Resources in Arunachal Himalaya' (Project No. DST/CCP/MRDP/ 185/2019(G) dated 13/03/2020). The project is supported by Department of Science & Technology (SPLICE – Climate Change Program), Ministry of Science and Technology, Govt. of India. The authors express their gratitude for receiving the financial support for the same. The authors are also thankful to Prof. Sreedeep Sekharan, Department of Civil Engineering, IIT Guwahati for providing technical support to understand some critical behavior of soil under unsaturated conditions

Compliance with Ethical Standards

Conflict of Interest: The authors declare that they have no known competing financial interests or personal relationships that could have appeared to influence the work reported in this paper.

Ethical Approval: This article does not contain any studies with human participants or animals performed by any of the authors.

Author Contributions: DA: Conceptualization, Formal analysis, Writing – Original preparation; AD: Supervision, Revision and Editing of drafted manuscript; RK: Supervision

Data Availability Statement: The data pertaining to and reported in this study is available from the corresponding author upon reasonable request.

Water Balance and Slope Stability in a Changing Climate: Combinatorial Influences of Rainfall and Snowmelt Induced Himalayan Geohazards

Abstract

Stability analysis of slopes and water balance studies in Indian mountainous regions under normal temperature conditions and rainfall are well explored. However, in cold regions such as the glaciated Himalayan areas, negative temperatures and snowmelt water play a crucial role in governing water dynamics and stability of terrain slopes. These aspects of cold region engineering are still in a very developing stage in India, despite the vulnerability of the Indian Himalayan regions to geohazards. The present study aims to address this gap by examining the effect of negative temperatures and snowfall during winters, and the influence of snowmelt water in addition to rainfall during summers, on stability of sloping terrain and the water balance dynamics in Indian Himalayan region. Slope profiles consisting of homogeneous soils and reconstituted varved clay slopes are utilized in the study, using two soil types, namely Red Soil (RS) and Black Soil (BS). The homogeneous slope profiles consist solely of either RS or BS. For reconstituted varved clay slope profiles, RS and BS are arranged in layers of 2, 4, 8, and 16 in two different sequential arrangements. In one sequential arrangement, BS constitutes the topmost lamina, whereas in the other, RS constitutes the topmost lamina. Results indicate that the slope failure, the area affected by failed soil mass, water infiltration into the sloping terrain, and runoff vary among different slope profiles. These variations are observed under different climatic scenarios, which include consideration of water from rain only (RW) and water from both rain and snowmelt (RW+SW). In the RW+SW climate scenario, early slope failures and increased water runoff are observed compared to RW. Accelerated water infiltration leads to earlier attainment of maximum cumulative infiltration and earlier runoff initiation in RW+SW scenario compared to RW. These output parameters also vary with the thicknesses and sequential arrangement of laminae in reconstituted varved clays slopes. For the same number of laminae, slope failure and maximum net cumulative infiltration occurs later when BS is the topmost lamina. Also, in this arrangement, the area affected by failed soil mass is also smaller compared to when RS is the topmost lamina with the same number of laminae.

Keywords: Slope Stability, Snowmelt Water, Finite Element Modelling, Reconstituted Varved Clays, Infiltration, Runoff

1. Introduction

Climate change induced global warming has been identified as a major reason for the rapid recession of glaciers in the Indian Himalayan Region (IHR) at an alarming rate (Rafiq *et al.*, 2016; Mir *et al.*, 2018; Chauniyal and Semwal, 2021). Climate change has caused severe impacts on both natural and human systems across the globe, and the associated geohazard risks are expected to continue to amplify (IPCC, 2014; Lagmay *et al.*, 2020). The difficulty in predicting such catastrophic events, along with inadequate preparedness at the time of their occurrence, is leading to loss of lives, environmental damage, and infrastructure destruction (Bhasin *et al.*, 2023). These events in cold regions have attracted significant global research attention. However, despite this global focus, studies in India that integrate geotechnical engineering with cold region sciences are still in their infancy and remain significantly underdeveloped.

The complex interaction between climate and land play a crucial role in slope stability in cold regions (Dijkstra and Dixon, 2010). In cold regions, these land-climate interactions involve the melting of glaciers and snow, mostly followed by thawing of frozen ground, which have been linked to an increased frequency of landslides due to climate change (Rist and Phillips, 2005). Disasters induced by adverse climate change, such as cloudburst-triggered flash floods, debris flows, mass movements, and landslides, are common phenomena in the Himalayas. Heavy precipitation, in combination with water from the rapid melting of snow, has also been reported to cause an increase in the number of geohazards in the Himalayas (Carey, 2005; Worni *et al.*, 2012; Mishra and Liu, 2014). The 2013 Kedarnath flood disaster serves as a prime example of a natural catastrophe triggered by snowmelt water, with heavy snowfall preceding the event in June. Scientific research suggests that intense rainfall accelerated the snowmelt in the upper region of Kedarnath, whose water combined with rainwater runoff to generate a massive flow of water which led to devastating debris flow (Martha *et al.*, 2013; Rao *et al.*, 2014; Singh *et al.*, 2015, Rafiq *et al.*, 2019). The role of water from snowmelt in the Uttarakhand disaster in 2021 was also found to be vital, with sudden floods capable of initiating landslides (Martha *et al.*, 2021; Kropáček *et al.*, 2021). Several other studies have identified a reduction in shear strength of sloping grounds due to the degradation of permafrost, melting of snow and glaciers, and ice-filled rock discontinuities which can lead to mass failures of sloping grounds (Seneviratne *et al.*, 2012). Although extensive research on climate change has been conducted, studies on its potential impact on water dynamics and stability of natural slopes is still lacking (Scaringi and Loche, 2022). In the glaciated mountainous regions of India, it is crucial to account for the effect of negative temperatures and water from snowmelt when examining water dynamics and slope stability. This study incorporates these factors by considering the influence of negative temperatures and snowfall during winter, along with the consequent snowmelt during summer.

Another important consideration in this study is the laminae structure within the selected terrain profile of the study area. Stability studies in layered slope profiles have recently gained significant attention from researchers due to the prevalence of multilayered soil compositions in natural and artificial slopes (Deng *et al.*, 2019; Chatterjee and Murali Krishna, 2021). Several studies have emphasized the profound impact of water infiltration processes in layered soil profiles as it is crucial in governing the stability of slopes (Damiano *et al.*, 2017). For instance, Dai *et al.* (2022) analyzed slope stability using silt and clay soils arranged in horizontal layers, focusing on the effect of lower layer thickness on the Factor of Safety (FoS). The study found that when clay overlaid silt, the FoS decreased as the silt layer thickness exceeded 0.2 times the slope height, while the opposite trend occurred with inverse layering. Groundwater level variations also affected slope stability, with FoS decreasing as groundwater lowered below the slope toe. Chatterjee and Murali Krishna (2021) used numerical modeling to study homogeneous and layered soil slopes. The findings revealed rotational failure in homogeneous fine-grained soils and translational failure in layered profiles with coarse-grained soil on top. FoS decreased with an increase in the thickness of the top layer when the bottom layer was stiff and increased when the top layer was stiff. From the discussed literature, it can be observed that the study of layered soil profiles is carried out considering horizontal layering. However, in reality, the layering may exist parallel to the sloping ground as well conforming to the depositional bedding planes. Moreover, the studies are based on either the insertion of a weak layer in a soil slope profile or considering a two-layered sloping soil profile; however, in practical conditions, there might be numerous layers in a deposit. The present study focuses on sloping ground constituting reconstituted varved clays. The study uniquely examines the effects of laminae sequence and the number of laminae on slope stability, infiltration, and runoff in the selected study area.

The Himalayas in Northeast India are highly vulnerable to landslides, and experience chronic economic losses worth billions of rupees due to a wide range of landslide issues (Reddy, 2014). Compared to other regions in Indian Himalayan belt, the Northeastern Indian Himalayas have seen a dearth of research on slope stability analysis (Dikshit *et al.*, 2020). The scarcity of research in the IHR is primarily attributed to the remoteness of this region and its challenging terrains (Kansal and Singh, 2022; Singh *et al.*, 2023). For the present research, the study area comprises Tawang glaciatic region, located in the Northeastern state of Arunachal Pradesh, India. Varved clays, common in glacial environments, are an example of naturally layered soils with alternating dark and light-colored bands (Anderson and Dean, 1988; Shur and Zhestkova, 2003; Netto *et al*., 2012; Palmer *et al*., 2019; de Vries *et al*., 2022; Vergnano *et al*., 2023; Wang *et al*., 2023) and have been observed in such glaciated Indian Himalayan regions as well (Ahmad and Hashimi, 1974; Pant et al., 1998; Juyal *et al*., 2009; Bhattacharyya *et al*., 2011; Beukema *et al*., 2011). In these regions, varved layers of varying thicknesses are commonly and frequently found to constitute the glaciatic slopes (Palmer *et al*., 2019). In the present study, the laminae structure of varved clay has been simulated by alternately and repetitively arranged two selected soils for the present study, namely Red Soil (RS) and Black Soil (BS). These soils were specifically chosen based on preliminary geotechnical investigations that identified their compatibility with the geotechnical properties of natural varved clay (the same is elaborated in subsequent section). The alternate arrangement of RS and BS, with varying thicknesses, is representatively used to simulate varved clays with diverse laminae thicknesses, thereby producing various configurations of slope sections. The present study advances the current knowledge by investigating the effect of alternatively arranged laminae soil structures, their sequential arrangements, and the additional water infiltration by snowmelt. The analysis includes an evaluation of FoS against slope failure using Morgenstern and Price (1965) method, along with cumulative net infiltration and cumulative runoff in all the slope profiles, while considering the influence of land-climate interaction. This interaction encompasses the application of water flux from rainfall, with and without the inclusion of water from snowmelt (RW and RW+SW). Additionally, the study investigates influence of the number of laminae in the reconstituted varved clays and their sequential arrangement on FoS, infiltration, and runoff dynamics.

In a nutshell, although the Himalayan territory has been quite well analysed in terms of the geohazards emanating from the rainfall or seismicity related triggers, hardly any studies exist until date that addresses the possible geohazards that can be triggered by seasonally infiltrating water emanating from rainwater and snowmelt in specific regions of such mountainous terrains of the Indian Himalayan system. Hence, this particular study provides an avenue to step beyond the existing state-of-the-art knowledge of instability in the glaciatic or sub-glaciatic Himalayan region.

2. Materials and Methodology

2.1 Material Characterization of Constituent Laminae

This study involves the utilization of two distinct soil types, namely Red Soil (RS) and Black Soil (BS), both of which were sourced from the vicinity of the IIT Guwahati campus (Figure 1). The suitability and justifiability of selecting these soils as couplet laminae simulants of actual varved clays has been ensured based on a comprehensive geotechnical investigation conducted in the laboratory. These geotechnical investigations included determining properties such as Atterbergs Limits (IS:2720 Part 5, 1985), Particle Size Distribution (IS:2720 Part 4, 1980) and compaction characteristics (IS:2720 Part 7, 1980) for both RS and BS. The table also includes the magnitudes of specific gravity (IS:2720 Part 3/Sec-2, 1980) and shear strength parameters obtained from direct shear tests (DST) conducted following ASTM D3080/D3080M (ASTM 2011). Table 1 lists the characteristic parameters of RS and BS relevant for the present study. The assessed parameters are found to be well within the ranges of the characteristic properties of actual varved clay layers that has been ascertained by several researchers in many literatures such as by Eden (1955), Kazi (1967), Eigenbrod and Burak (1991), Lydzba and Tankiewicz (2012), Florkiewicz *et al.* (2014), Tankiewicz (2016), Krawczyk and Szymanska (2018), and Flieger-Szymanska *et al.* (2019). Thus, the laboratory analyses revealed that RS can effectively simulate the light-colored, silt-dominant laminae found in actual varved clays, while BS can serve as a representative of the darker, clay-dominant laminae; and the same has been adopted for the present study.

Figure 1. Representative sample of **(a)** RS and **(b)** BS collected in the vicinity of IIT Guwahati campus

Table 1. Geotechnical properties of RS and BS

Geotechnical Parameters	Red Soil (RS)	Black Soil (BS)
Specific Gravity	**2.7**	**2.6**
Atterberg Limit (%)		
Liquid Limit	45	95
Plastic Limit	19	30
Plasticity Index	26	65
Compaction Characteristics		
Maximum Dry Density (g/cc)	1.77	1.59
Optimum Moisture Content (%)	19.5	21.5
Grain Size Distribution (%)		
Sand	23.2	8.4
Silt	54.4	6.7
Clay	22.4	84.9
Soil Classification	ML	CH
Shear Strength Parameters		
Effective friction angle (°)	17.53	13.0
Cohesion (kPa)	12.4	6.1

After selecting RS and BS, as mentioned above, several other laboratory tests were conducted to obtain input parameters for conducting the numerical modelling for the present study. These tests included the estimation of saturated hydraulic conductivity, data points for calculating unsaturated hydraulic conductivity properties, and shear strength parameters for the two chosen soils. Saturated hydraulic conductivity was determined in the laboratory using pre-fabricated permeability mould whose dimensions were in accordance to the standards outlined in ASTM-D5856-15 (ASTM 2015). To obtain unsaturated parameters for both RS and BS, data points for the Soil Water Characteristic Curve (SWCC) were acquired using a WP4-T Dew Point Potentiometer manufactured by Decagon Devices, Inc., Pullman, WA, USA (Figure 2). The SWCC represents the relationship between water content in soil at different suction magnitude and is crucial in predicting the water movement through soil. The data points obtained through the potentiometer consists of various suction values corresponding to different moisture contents. The working principle of the potentiometer can be found in detail in ASTM D6836 Method D (ASTM 2002). These data points were then fitted to the van Genuchten model (van Genuchten, 1980) to obtain smooth SWCC of both soils. Equation 1 represents the van Genuchten formulation used for obtaining SWCC (van Genuchten, 1980). Subsequently, the van Genuchten model parameters were further utilized to derive Hydraulic Conductivity Function (HCF) curves for RS and BS. HCF represents the variation of hydraulic conductivity with matric suction of soil or its degree of saturation. Equation 2 represents the equation used for deriving HCF curve.

$$\theta = \theta_r + \frac{\theta_s - \theta_r}{[1+|\alpha h|^n]^m} \quad (1)$$

$$K(h) = \frac{K_s\{1-(\alpha h)^{mn}[1+(\alpha h)^n]^{-m}\}^2}{[1+(\alpha h)^n]^{ml}} \quad (2)$$

where θ represents the volumetric water content in soil (m^3/m^3); θ_r and θ_s represents the residual and saturated volumetric water content (m^3/m^3) of the soil respectively; K_s and $K(h)$ is the saturated and unsaturated hydraulic conductivity (m/s). The parameters α, m and n are empirical parameters, where m is calculated as $(1 - {}^{1}/_{n})$.

Table 2. van Genuchten parameter, water content, permeability and shear strength parameters of RS and BS

Parameters	Red Soil (RS)	Black Soil (BS)
van Genuchten Parameters		
a (kPa)	167	1000
n	2.6	1.8
m	0.615	0.444
Water Contents		
Saturated Volumetric Water Content, θ_s (m^3/m^3)	0.42	0.37
Residual Volumetric Water Content, θ_r (m^3/m^3)	0.035	0.045
Saturated Permeability, K_s (m/s)	1.10x10^{-7}	5.18x10^{-9}

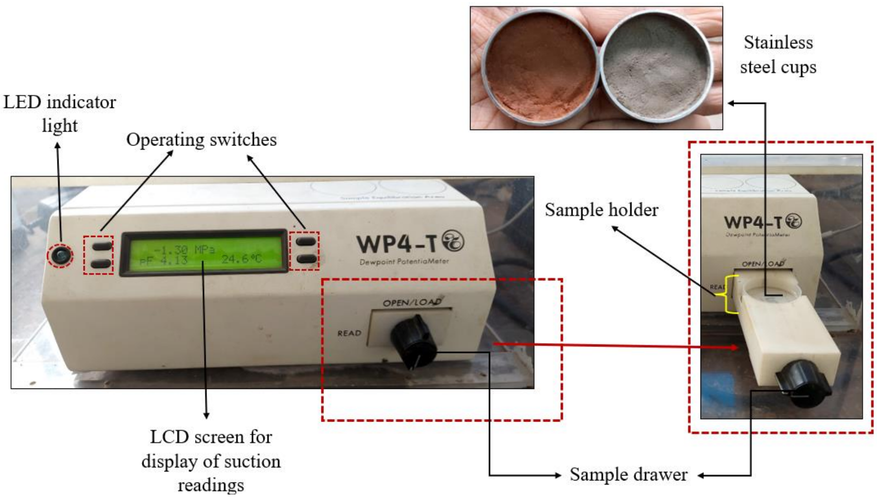

Figure 2. WP4-T Dewpoint Potentiometer with its operating parts, and prepared soil sample in stainless steel cups

The fitted SWCC and the data points for RS and BS are illustrated in Figure 3(a). Subsequently, the Van Genuchten parameters, in conjunction with the saturated hydraulic conductivity (K_s), were utilized to calculate HCF curves for both RS and BS, following Equation 2. The HCF curves for both soils are depicted in Figure 3(b).

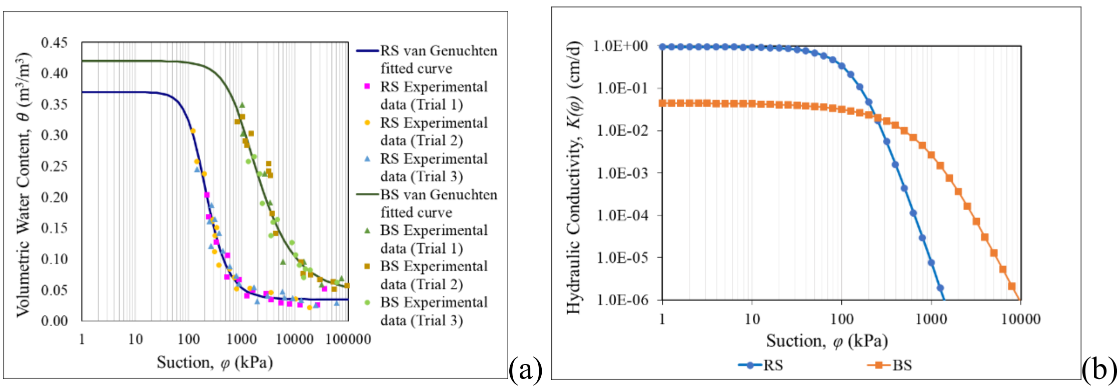

Figure 3. (a) Soil Water Characteristic Curve for RS and BS **(b)** Hydraulic Conductivity Function curve for RS and BS

2.2 Methodology and Numerical Modelling

Figure 4 shows the terrain profile from the Indian Himalayan Region of Tawang considered in the present study. The terrain data (Figure 4b) is extracted from Google Earth (Figure 4a) image of the location. From the figure, it can be observed that there are infinite sets of slip surface possible for the chosen terrain. Additionally, there is an infinite number of slope angles present in the study terrain profile. Therefore, conducting slope stability analysis for the entire stretch of the terrain is not feasible. Instead, a location is selected on the terrain profile for conducting slope stability analysis based on its high sensitivity to hydrological variation during ground-climate interaction. From the water pressure profile of the terrain during the study period, it is observed that there is a rapid decrease in initial negative water pressure at the chosen marked location in Figure 4. This indicates a rapid rate of suction loss at this terrain section. Such a phenomenon may be attributed to the additional downward infiltration of water from the upper mountain region. The loss of suction due to water infiltration leads to the destabilization of the slope. Additionally, the figure shows that the marked section has a steep sloping terrain for a sufficient length. Steeper slopes have a higher tendency to undergo sliding. The inclination of the sloping ground and the hydraulic characteristics of the soil govern the amount of infiltration into the soil, the corresponding runoff and the FoS of the slope. The rapid decrease in suction combined with a steep and extended soil slope length makes the selected topography appropriate for carrying out slope stability analysis.

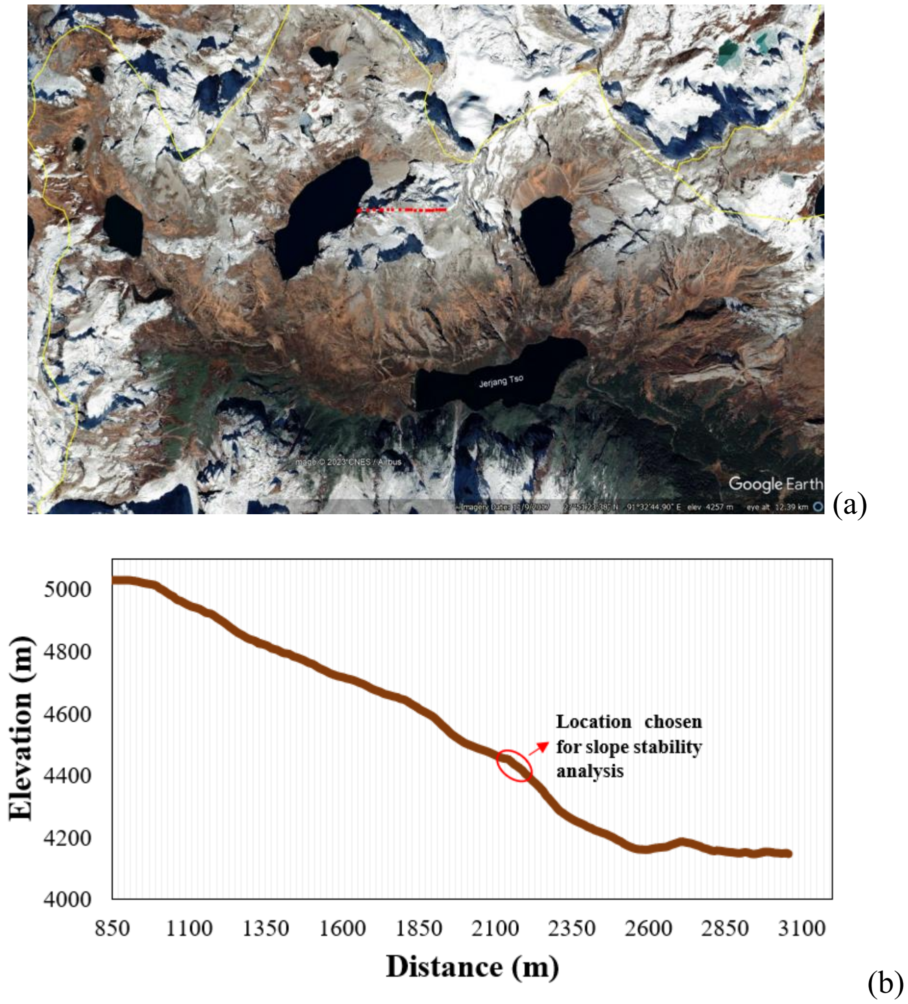

Figure 4. (a) Google earth image of the Tawang study area (b)Terrain profile extracted from Google earth image for hydrological study with marked location for slope stability analysis

For homogeneous soil terrain profiles, two profiles are created individually with RS and BS. In case of reconstituted varved clay in the same sloping terrain, the two selected soils are arranged in layers of the same total thickness (400 cm) as considered for homogeneous soils. The reconstituted varved clay slope profile is considered in two types of sequential arrangements. In one set of laminae arrangements, BS occupies the topmost lamina, while in the other set, RS serves as the topmost lamina. Both types of laminae arrangements are considered in the present study because the characteristics of slope failure, infiltration, and runoff will be different in both cases. The interaction of the topmost lamina is pivotal, as the land-climate interaction of the sloping terrain primarily occurs through that lamina. Notably, the alternating laminae arrangement in the varved clay soils introduces variability in soil properties across its vertical profile. The laminae structures also govern moisture distribution, which influences the slope stability mechanisms. The sloping terrain comprising reconstituted varved clay with BS as the topmost layer is designated as 2L_BS, 4L_BS, 8L_BS, and 16L_BS, where 'L' represents 'Lamina', and the numeric digits indicate the number of laminae. Similarly, for RS lying at the top, the reconstituted varved clays are represented as 2L_RS, 4L_RS, 8L_RS, and 16L_RS.

The present study assumes a constant active region depth of 400 cm throughout the considered terrain (Figure 6). The active region depth of 400 cm is determined by the findings of several researchers, who have identified it as the optimal depth for maximum infiltration, water storage, and moisture fluctuation (Zou *et al.*, 2001; Dongli *et al.*, 2014; Mei *et al.*, 2018; Luo *et al.*, 2023; Ya *et al.*, 2023). This active region depth signifies the maximum depth until which the water flux can infiltrate in glaciatic region, thereby affecting the slope stability of the varved slopes until this depth. Therefore, active region depth represents the maximum soil depth affected by hydrological processes such as freezing, thawing and infiltration. In this study, numerical modeling is carried out using GeoStudio 2023.1.0. The SEEP/W and SLOPE/W modules of GeoStudio are integrated for carrying out transient analysis for 365 days. The coupling of SEEP/W and SLOPE/W allows for the simulation and analysis of the complex dynamics between infiltrating water, runoff, and slope stability with a time increment of 0.2 days. The SEEP/W module is configured to simulate transient water flow through unsaturated and saturated soils under varying climatic conditions. This module follows Darcy's law to govern water flow through porous media. The model incorporates SWCC and HCF for both RS and BS. The boundary condition at the top of the sloping ground consists of time-varying water flux along with other climatic variables. While the water is free to move in lateral directions, such as down the slope, it is restricted to flow beyond 400 cm depth as discussed previously.

In this study, slope stability analysis is performed using the Morgenstern and Price (1965) method. For the homogeneous sloping terrain profiles, the slip surface assessment is determined by the entry-exit method, whereas for reconstituted varved clay profiles, the block-specified method is used (Figure 6). In both of these methods, a certain number of trial slip surfaces are generated, and the slip surface with the minimum FoS is selected as the critical slip surface. In Figure 6(a) and 6(b), the red line along the ground surface in homogeneous RS and BS soil profiles represents the entry (left side) and exit zones (right side). In Figure 6(c) to 6(f), green-colored grids can be seen throughout the depth of the soil profiles when the block specified method of generation of slip surfaces is used. These grids are referred to as the left block and right block. In both of these cases, the direction of trial slip surface generation aligns with the direction of slope failure, i.e. from left to right. The block-specified search technique method of slope stability is best suited when there is a presence of a low-strength layer in the slope profile and the middle segment line between the two grids is significantly longer than the projection segment at both ends. In the present study, the two chosen soils are arranged in a different number of layers, with BS having lesser strength parameters than RS. Therefore, the block-specified method is used in the case of layered soil slope profile. Furthermore, while the vertical lines in both the grids are taken as 11 for all the layered soil slope profiles, the number of horizontal lines in the grid is determined according to the number of laminae constituting the slope profile. If N is the number of layers, then the number of grid lines in the horizontal direction is taken as N+1. This is done to ensure that the horizontal grid line lies at the top and bottom of the sloping profiles and at the interface of RS and BS. Therefore, the number of horizontal lines in both left and right grid is 3, 5, 9, and 17 for 2-Layered, 4-Layered, 8-Layered, and 16-Layered reconstituted varved clay slope profiles. In homogenous soil slope cases where the entry-exit method is used, 11 entry and exit points are used. In Figure 6(c), 6(e), 6(g), and 6(i), the reconstituted varved clay slope profile with BS as the topmost lamina is shown. A similar type of arrangement is done for the analysis when RS occupies the topmost layer, as depicted in Figure 6(d), 6(f), 6(h), and 6(j).

The analysis covers a total study period of 365 days, beginning in November and ending in October of the succeeding year. The present study utilizes ten years of average real-time meteorological data of Tawang in the state of Arunachal Pradesh, India. This data is obtained from an online climate data collector (World Weather Online). Initially, it is assumed that there is no snow on the ground, and the soil profiles have an initial pressure of -1500 kPa. The meteorological data, including air temperature, humidity, wind speed, and precipitation, are averaged over a month. Months with an average temperature equal to or below 0°C are considered winter months (November to March), while those with a positive average air temperature are considered summer months (April to October). The study assumes that precipitation occurs as snow during winter and as rainfall during the summer season. The analysis starts in November, marking the onset of the winter season during which the precipitation occurs as snow. Snow simply accumulates on the soil surface from day 0 to day 151 (November to March). Day 152 marks the start of April and hence the onset of summer season. In summer season, precipitation occurs as rainfall. The present study considers infiltration under two different climatic conditions of RW and RW+SW. In terms of albedo, it varies from 0.9 for freshly fallen snow to about 0.2 for dirty snow, and during melting, the albedo is around 0.4 (Hall and Martinec, 1985). In this study, an albedo of 0.9 is considered for winter months when it snows (days 0 to 151, November to March), and an albedo of 0.4 is considered for summer months when snow is melting (days 152 to 365, April to October).

2.2.1 Land-Climate-Interaction (LCI) Boundary Conditions

In cold region geotechnical engineering studies that incorporate the impact of climate change, it becomes crucial to consider interactions between the various components of the atmosphere and near-surface soil (Tang *et al.*, 2018). These interactions help in understanding the behaviour of geo-structures in these cold areas. Therefore, this study incorporates Land-Climate-Interaction (LCI) boundary conditions, which considers water dynamics along the depth of the soil due to climate variability (Nunes *et al.*, 2022). LCI boundary conditions incorporate climate data such as air temperature, precipitation, relative humidity, wind speed, solar radiation, and albedo. Solar radiation is estimated based on the specific day of the year and the latitude of the study area. For the present study, the latitude of the study area is 27.84542°.

During winter, snow accumulates on the ground surface, resulting in no net infiltration into the ground. Since no infiltration occurs, there is no change in pore water pressure within soil, and consequently, no change in the FoS of the sloping terrain during this period. However, as temperatures rise above freezing (T > 0°C) in the summer, the accumulated winter snow begins to melt. This melted snow, referred to as Snow Water Equivalent, represents the water stored in a snowpack. Snow Water Equivalent is crucial for water balance studies, including its application in geotechnical engineering, as it affects the stability of slopes due to variations in pore water pressures. Snow Water Equivalent at the current numerical time step (SWE_t) (mm/day) is calculated using Equation 3.

$$SWE_t = SWE_{t-1} + SF - SM \quad (3)$$

where SWE_{t-1} is the snow water equivalent at the previous numerical time step (mm/day), SF is the snowfall precipitation rate and SM is the snowmelt rate (mm/day).

The snowmelt rate is calculated using Equation 4, as proposed by the U.S. Army Corps of Engineers (U.S. Army COE, 1998). This equation utilizes an energy balance approach to determine the rate of snow melting. It is important to note that there are two separate equations available to calculate the rate of snow melting, one for rainy days and one for non-rainy days. In the present study, the equation for rainy days is used since the analysis considers the average precipitation throughout the given month. Therefore, Equation 4 is applied to calculate the rate of snowmelt in this study.

$$SM = C[0.09 + (0.029 + 0.00504v + 0.007P)(T_a - T_F)] \quad (4)$$

where v is the wind speed (miles/hr), T_a is the air temperature (°F), T_F is the freezing temperature (°F) that is considered as 32°F in the present study, and C is the coefficient to account for variations that is assumed as 2.5 in the present study. This choice of C is based on several factors, including the non-linear and diverse nature of snowmelt-related variables. This value of 2.5 is supported by findings from various studies (Burakov and Ivanova, 2010; Liu *et al.*, 2015; Davenport *et al.*, 2019; Ruijsch *et al.*, 2021), which collectively demonstrate the substantial variability in snowmelt processes and their significant impact on hydrological responses.

As stated above, the Snowfall (SF) precipitation is calculated based on given temperature during the particular time which is represented numerically as given in Equation 5.

$$SF = Q_p \times P \quad (5)$$

where *P* is the precipitation (mm/day), and Q_p is the thermal factor given in Equation 6:

$$Q_p = 0 \ (if\ T_a > T_f);\ Q_p = 1 \ (if\ T_a < T_f) \quad (6)$$

2.2.2 Slope Stability and Shear Strength of Soil under Unsaturated Conditions

In the present study, the slope stability analysis employs the Mohr-Coulomb material model in an unsaturated state. This particular model, which was proposed by Vanapalli *et al.* (1996), is based on Bishop's effective stress principle, and is described using Equation 7.

$$\tau = c' + (\sigma_n - u_a)tan\phi' + (u_a - u_w)[\chi tan\phi'] \qquad (7)$$

where τ is shear strength of soil (kPa), σ_n is net total stress (kPa), $u_a$is pore air pressure (kPa), c' is effective cohesion (kPa), ϕ' is effective angle of internal friction (°) and χ is parameter related to the degree of saturation.

χ is defined by Vanapalli *et al.* (1996) as:

$$\chi = \frac{\theta_w - \theta_r}{\theta_s - \theta_r} \qquad (8)$$

In the present study, slope stability analysis is performed using the limit equilibrium technique proposed by Morgenstern and Price (1965). This method employs FoS equations with respect to the moment equilibrium (FoS_m) and with respect to force equilibrium (FoS_f), as provided in Equation 9 and Equation 10, respectively.

$$FoS_m = \frac{\sum[c'lR + \{N - u_w l\chi - u_a l(1-\chi)\}Rtan\phi']}{\sum Wx - \sum Nf \pm \sum Dd \pm \sum Aa} \qquad (9)$$

$$FoS_f = \frac{\sum[c'lcos\alpha + \{N - u_w l\chi - u_a l(1-\chi)\}tan\phi' cos\alpha]}{\sum Nsin\alpha - \sum Dcos\omega \pm \sum A} \qquad (10)$$

where W is total weight of a slice of width b and height h, N is total normal force on the base of the slice, D is external point load, R is radius of a circular slip surface or moment associated with the mobilized shear force, x is horizontal distance from the centreline of each slice to the centre of rotation or to the centre of moments, d is perpendicular distance from a point load to the centre of rotation or to the centre of moments, a is perpendicular distance from the resultant external water force to the centre of rotation or to the centre of moments, A is resultant external water forces, ω is angle of the point load from the horizontal, α is angle between the tangent to the centre of the base of each slice and the horizontal and l is base length of each slice.

In the present study, the mobilized shear and normal stresses in unsaturated states are determined using Equation 11 and Equation 12, as proposed by Fredlund and Krahn (1977).

$$\tau_m = \frac{l}{F}(c' + (\sigma_n - u_a)tan\phi' + (u_a - u_w)tan\phi^b \qquad (11)$$

$$N = \frac{W + (X_R - X_L) - [\frac{c' + lsin\alpha + u_a bsin\alpha\left(tan\phi' - tan\phi^b\right) + u_w lsin\alpha tan\phi^b}{F}}{cos\alpha + \frac{sin\alpha tan\phi'}{F}} \qquad (12)$$

where τ_m is shear force mobilized on the base of each slice, and F is horizontal interslice normal forces. Subscript L and R designate the left and right sides of the slice, respectively.

In the present study, a relationship is derived by equating the unsaturated soil shear strength equations proposed by Vanapalli *et al.* (1996) and Fredlund *et al.* (1978) as given in Equation 13.

$$tan\phi^{b} = \chi tan\phi' \quad (13)$$

In the present study, the inclination angle of slopes and the change in pore-water pressure due to water infiltration are the driving forces, whereas the shear force generated along the slip surface acts as the resisting force. In slope stability analysis, FoS is a measure of the ratio of resisting forces to driving forces on a slope. As soon as the FoS drops below 1, the slope becomes unstable and eventually fails. An FoS equal to 1 signifies that the resisting forces just become insufficient to counteract the driving forces, which marks the onset of slope instability. Therefore, an FoS equal to 1 signifies the imminent stable slopes under ideal conditions when no uncertainties are considered. However, in reality, there are significant uncertainties associated with shear strengths around the failure plane. Therefore, under static conditions of slope stability, an FoS of 1.5 (as per IS14243 Part 2: 1995) is commonly adopted to ensure a safety margin for slopes. Consequently, the present section discusses the FoS trends for all ten considered soil profiles under two different climate conditions of RW and RW+SW. The day on which the FoS drops just below 1.5 is also discussed, and the area under the failed soil slope mass is analyzed for different soil slope profiles.

3. Results and Discussions

This section presents the results obtained from the study for various combinations of two climatic conditions (RW, RW+SW) and ten slope profiles (RS, BS, 2L_BS, 4L_BS, 8L_BS, 16L_BS, 2L_RS, 4L_RS, 8L_RS, 16L_RS). The section is further divided to discuss how these variables impact the FoS and area of the soil profile affected by slope failure in Section 3.1, and water dynamics in Section 3.2 across the considered slope profiles. It should be noted that, although the study period spans 365 days, the graphical plots for FoS and cumulative net infiltration over time represent data for a limited time frame, as the values remain constant beyond these intervals.

3.1 Variation in FoS in Different Soil Profiles for RW and RW+SW Scenarios

The graphical plots in Figure 5(a) to 5(j) show the change in FoS over time. For all the slope profiles, a decrease in FoS during the summer season is observed. This decrease is attributed to the loss of soil strength, which is caused by a reduction in soil suction due to water infiltration. The rate of decrease in FoS in all slope profiles is relatively higher under RW+SW conditions, as the additional water from snowmelt leads to greater water infiltration into slope compared to RW. This results in earlier slope failure under RW+SW conditions. The exact day of failure for different soil profiles under various climate scenarios can be found in Table 5.

From Figure 5(a) and Figure 5(b), it is observed that the rate of decline in FoS is much more rapid in the case of homogenous BS slope profile compared to RS slope profile for both RW and RW+SW. Furthermore, slope failure occurs earlier in BS than in RS, even though the initial FoS for the BS slope profile is approximately 7.6 times higher than the initial FoS for the RS slope profile. The initial high FoS of the BS slope profile can be attributed to the higher χ parameter due to a higher difference in saturated volumetric water content (θ_s) and residual volumetric water content (θ_r), which significantly influences the shear strength of the soil (Equation 7). The values of θ_r and θ_s for both RS and BS are mentioned in Table 2. The initial suction is higher than the Air Entry Value (AEV) of RS and BS (Figure 3b and Table 2). The rapid rate of decrease in FoS in the BS slope profile, compared to RS slope profile, is due to the higher unsaturated hydraulic conductivity of BS at the high initial suction magnitude of -1500 kPa. From Figure 3(b), it is evident from the HCF curve that the saturated and near-saturated hydraulic conductivities for RS are greater than those for BS. However, beyond the intersection of the HCF curves for RS and BS, the trend changes, with BS exhibiting higher hydraulic conductivity than RS. This intersection point is referred to as the 'breakthrough suction point'. Therefore, as the hydraulic conductivity of BS is higher for the considered initial suction in the slope profile, there is a higher rate of water infiltration in BS slopes compared to RS slope profiles. This leads to the early attainment of saturation in BS slope profiles. Consequently, slopes consisting of BS fail earlier than those constituting RS.

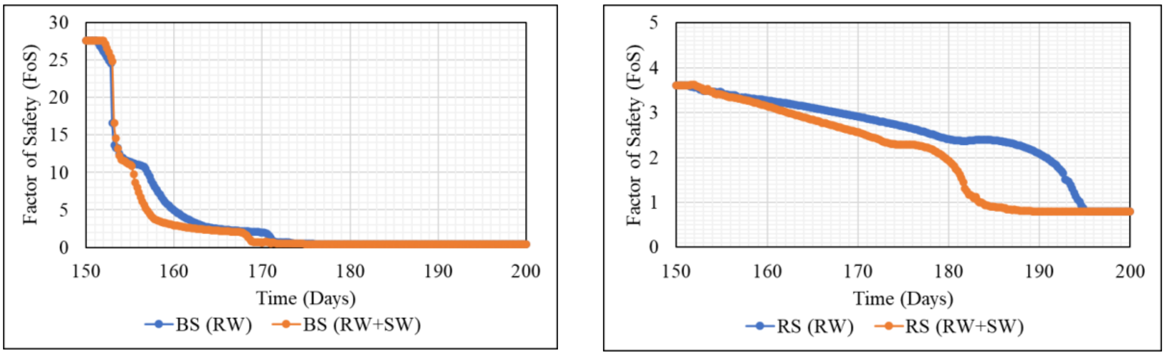

(a) **(b)**

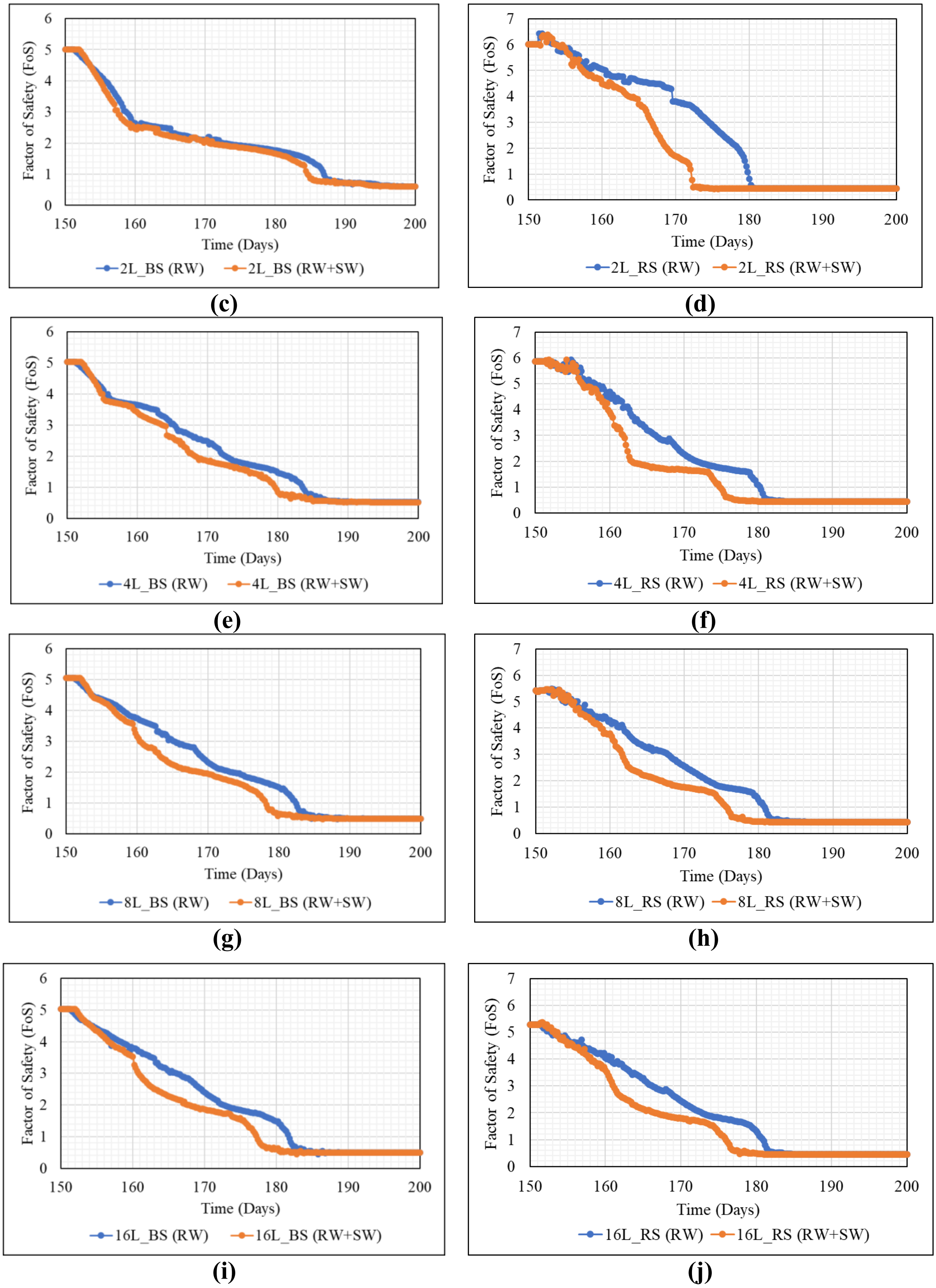

Figure 5. Variation in FoS in slope profiles for RW and RW+SW scenarios (a) BS (b) RS (c) 2L_BS (d) 2L_RS (e) 4L_BS (f) 4L_RS (g) 8L_BS (h) 8L_RS (i) 16L_BS (j) 16L_RS

Figures 5(c), 5(e), 5(g), and 5(i) show the change in FoS with time for soil slope profiles where the topmost lamina is BS, arranged alternately with RS in 2 layers, 4 layers, 8 layers, and 16 layers. Similarly, Figures 5(d), 5(f), 5(h), and 5(j) show the change in FoS with time for slope profiles where RS is the topmost lamina, arranged alternately with BS in 2 layers, 4 layers, 8 layers, and 16 layers. The figures show that the impact of additional water from snowmelt along with rain (RW+SW) is more pronounced in laminae slope profiles with RS as the topmost layer compared to those with BS as the topmost lamina. This is evident from the larger difference in FoS magnitudes between RW and RW+SW when RS is the topmost layer. Additionally, the graphs indicate that all the reconstituted varved clay slopes fail earlier when the topmost lamina is RS in both the RW and RW+SW cases. The days on which all slope profile, including the reconstituted varved clay slopes fails are listed in Table 3. It can be observed from the table that for the same number of laminae, slope failure occurs at different times depending on the sequential arrangements of laminae in reconstituted varved clay slope profiles. Slope profiles with RS as the topmost lamina fail earlier compared to those with BS as the topmost lamina. Another observation from Table 3 is that for reconstituted varved clay profiles with BS as the topmost layer, earlier failure in soil slopes is observed as the number of laminae increases in both RW and RW+SW cases. In contrast, for profiles with RS as the topmost layer, a reverse trend of delayed slope failure is observed as the number of laminae increases in both climatic conditions. The last column of Table 3 shows the time difference RW and RW+SW climatic conditions when the different slope profile fails. The difference in days when slope failure occurs between RW and RW+SW increases with the number of laminae for profiles with BS as the topmost lamina, whereas a decreasing difference in failure days is observed as the number of laminae increases for slope profiles with RS as the topmost lamina. This indicates that the rate of incoming water flux affects different slope profiles differently, depending on the sequential arrangement of the two laminae. The variation in the time of failure of slopes between the two sequential arrangements of reconstituted varved slopes is linked to the time taken to attain maximum cumulative net infiltration in each arrangement, as discussed in detail in Section 3.3 of the paper.

Table 3. Time (in days) when FoS drops below 1.5

Soils	Slope Profiles	RW	RW+SW	RW-(RW+SW)
Homogenous	RS	193.0	181.6	11.4
	BS	171.0	168.4	2.6
Reconstituted Varved Clay with BS as topmost lamina	2L_BS	184.6	182.2	2.4
	4L_BS	180.0	176.0	4.0
	8L_BS	180.0	175.6	4.4
	16L_BS	179.8	175.6	4.2
Reconstituted Varved Clay with RS as topmost lamina	2L_RS	178.6	171.4	7.2
	4L_RS	179.0	173.6	5.4
	8L_RS	179.4	174.2	5.2
	16L_RS	179.4	174.4	5.0

Figure 6 shows the failed slopes in the different slope profiles considered in the study. Figures 6(a) and 6(b) depict the critical slip surfaces formed during slope failure in the homogeneous BS and RS slope profiles, respectively. It is observed that the depth of the slip surface in the homogeneous RS slope profile is greater than in the homogeneous BS slope profile. This can be attributed to the lower cohesion and internal angle of friction of BS, which prevents it from sustaining large stresses due to increased pore water pressure, causing it to fail at a shallower depth compared to RS. In other words, since RS has higher magnitudes of shear strength parameters and the χ parameter does not hold significance for soils approaching saturation, RS is more resistant to shear failure compared to BS. Therefore, the RS slope profile is able to maintain stability at a greater depth before failing, as it can sustain higher stresses. However, the area of soil mass involved in failure is larger in the homogeneous RS slope profile compared to the BS slope profile, with the affected area measuring 52 m^2 for the homogeneous RS slope profile and 38.96 m^2 for the homogeneous BS slope profiles.

From the water pressure profile diagrams of the considered slope profiles, it is observed that slope failure occurs when a particular soil slope portion becomes fully saturated. Full saturation occurs when the soil reaches its maximum water-holding capacity, meaning all pores are filled with water, leaving no available air voids. This fully saturated section acts as a weaker zone than the rest of the soil mass, bounded by the propagating slip surfaces, one of which fully develops into the critical slip surface (Figure 6). Figures 6(c), 6(e), 6(g), and 6(i) show the critical slip surfaces in reconstituted varved clay laminae with 2, 4, 8, and 16 layers, respectively, where BS is the topmost lamina. Similarly, Figures 6(d), 6(f), 6(h), and 6(j) show the corresponding profiles where RS is the topmost lamina. It is observed from Figure 6 that in homogeneous slope profiles, the failure surface is circular, whereas in reconstituted varved clay slope profiles, the slip surface formed is transitional. A common observation in both sequential arrangements is that the maximum depth of the critical slip surface passes through the lowermost BS lamina. Since in 2L_RS, 4L_RS, 8L_RS, and 16L_RS, BS forms the lowermost lamina, slip surface penetrates the full 4 m thickness. For slope profiles with BS constituting the topmost lamina, the critical slip surface passes through Layer 1, Layer 3, Layer 7, and Layer 15 in the 2L_BS, 4L_BS, 8L_BS, and 16L_BS slope profiles, respectively. As a result, the critical slip surface forms at shallower depths when BS is the topmost lamina, leading to a smaller affected area of failed soil mass compared to when RS is the topmost lamina for the same number of layers. The area of soil mass involved in failure is 33.07 m^2 for 2L_BS, 51.38 m^2 for 4L_BS, 69.09 m^2 for 8L_BS, and 72.04 m^2 for 16L_BS. In comparison, for 2L_RS, 4L_RS, 8L_RS, and 16L_RS profiles, the affected areas are 78.16 m^2, 121.81 m^2, 79.89 m^2, and 84.08 m^2, respectively.

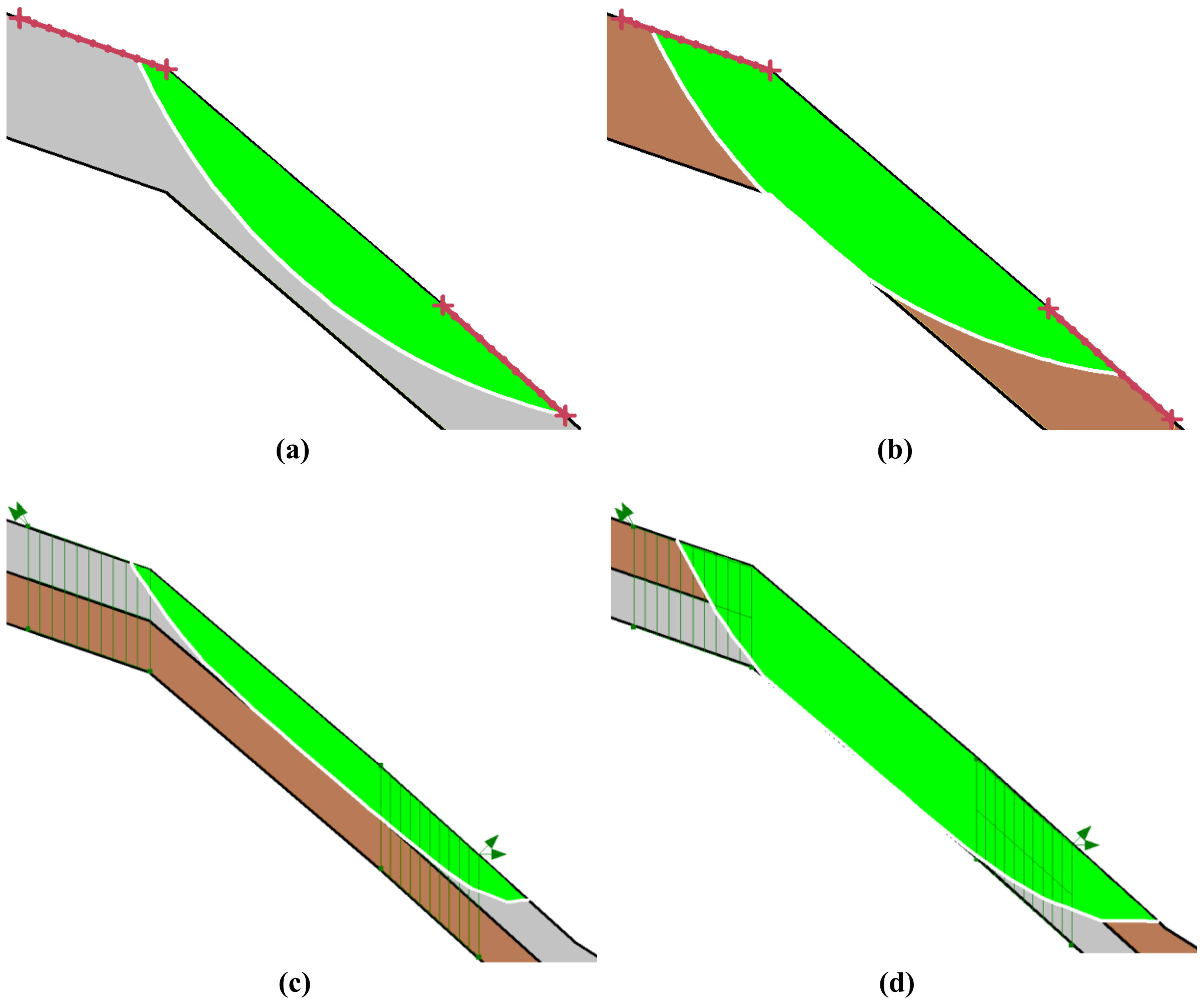

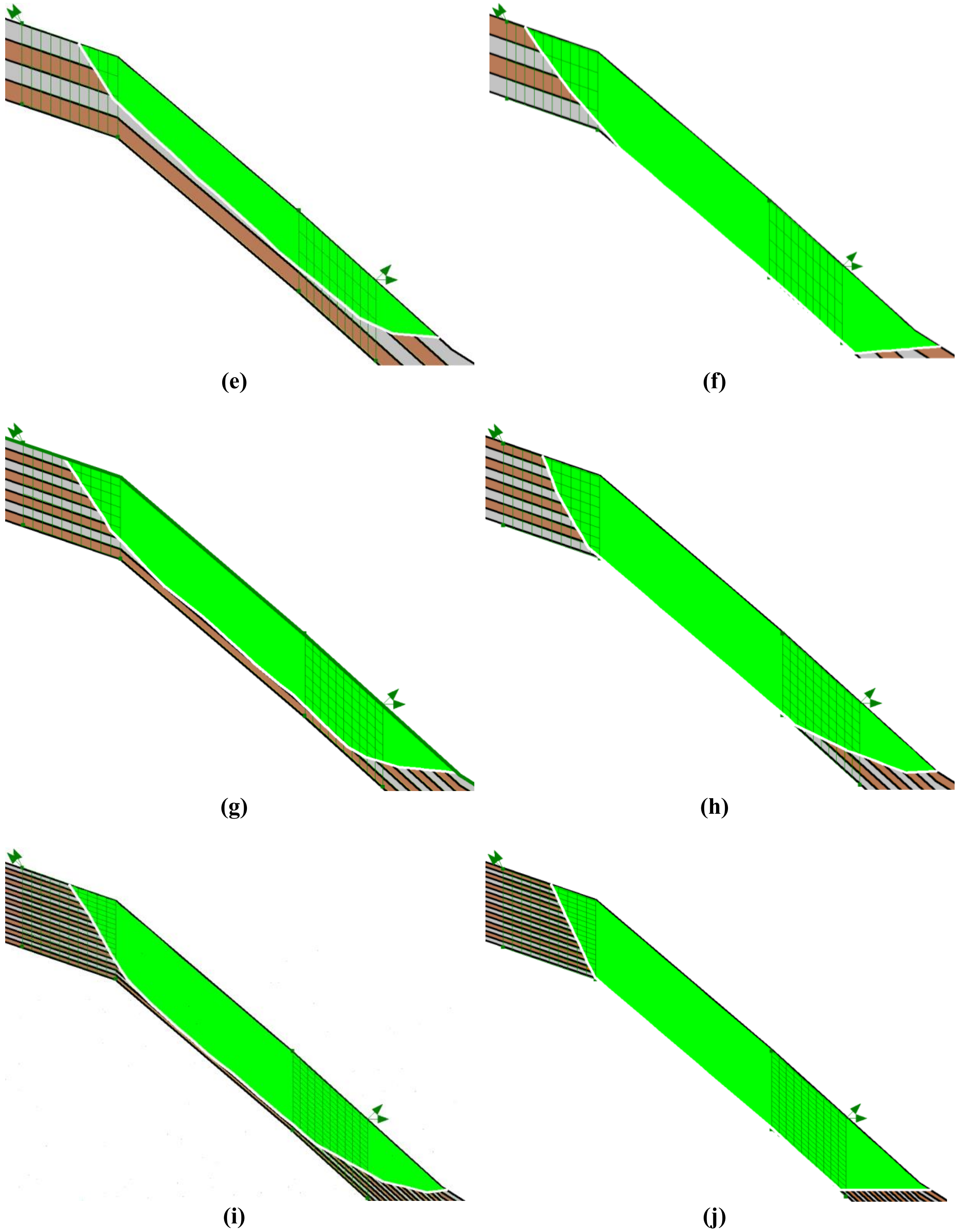

Figure 6. Failed soil mass enclosed in critical slip surface for various slope profiles (a) BS (b) RS (c) 2L_BS (d) 2L_RS (e) 4L_BS (f) 4L_RS (g) 8L_BS (h) 8L_RS (i) 16L_BS (j) 16L_RS

3.2 Cumulative Net Infiltration and Cumulative Runoff in Different Soil Profiles for RW and RW+SW scenarios

Figures 7(a) to 7(j) depict cumulative net infiltration over time for different soil slope profiles under both RW and RW+SW climatic conditions. Infiltration begins in all soil profiles under both climatic conditions with the onset of summer at 151 days. After some time, the infiltration rates in all soil profiles reach their maximum values and remain constant for the remainder of the study period up to 365 days. Although the rate of cumulative net infiltration differs between RW and RW+SW initially, both eventually converge to similar values in all the slope profiles. The graphical plots clearly show that cumulative net infiltration is higher under RW+SW conditions, due to the additional water from snowmelt combined with rainfall. Among the profiles, RS exhibits the highest cumulative net infiltration at 2793.28 m^3, while BS displays the lowest at 1309.91 m^3. Intermediate values are observed for all reconstituted varved clay profiles with different sequential arrangements. These infiltration values for different profiles are listed in Table 4. The larger value of the infiltration in RS compared to that in BS is due to the higher value of porosity 0.42 m^3/m^3 while the porosity of the BS is 0.37 m^3/m^3. Due to high porosity, more water volume can be stored in RS, resulting in a higher magnitude of maximum cumulative net infiltration. Conversely, lower porosity of BS allows for lesser water storage, leading to the lowest maximum cumulative net infiltration among all considered slope profiles. Among homogeneous soil profiles of RS and BS, cumulative net infiltration in the RS slope profile is more affected by the addition of snowmelt water compared to BS (Figures 7a and 7b). For reconstituted varved clay profiles, this additional water from snowmelt water has a greater impact on profiles with RS as the topmost lamina (Figures 7c to 7j). This is evident from the difference in magnitudes of cumulative net infiltration over the same time period before the curves for RW+SW and RW curves converge. Table 5 provides valuable insights into the time when the maximum cumulative net infiltration is achieved and stabilizes for the remainder of the study period. This information is crucial for understanding the dynamics of water infiltration and its impact on slope stability, particularly in the context of additional water from snowmelt. It can be observed that in the case of RW, the maximum and minimum durations to achieve cumulative net infiltration are for homogeneous RS and BS slope profiles, respectively. From Table 3, it can be observed that the maximum and minimum durations for soil failure are taken by homogeneous RS and BS sloping profiles, respectively. Similarly, in the case of RW+SW, the maximum and minimum durations to achieve maximum cumulative net infiltration are by 2L_BS and homogeneous BS slope profiles (Table 5). Correspondingly, 2L_BS and homogeneous BS take the maximum and minimum durations to fail (Table 3).

These observations indicate that water infiltration controls the failure of slopes. The more days taken to attain maximum cumulative net infiltration in a soil slope profile, the later the slope failure will occur. From Table 5, it can further be observed that the duration to attain maximum infiltration in 2L_BS, 4L_BS, 8L_BS, and 16L_BS is higher compared to 2L_RS, 4L_RS, 8L_RS, and 16L_RS, under both RW and RW+SW conditions. This trend aligns with the pattern of time to slope failure, with 2L_BS, 4L_BS, 8L_BS, and 16L_BS slopes failing later than 2L_RS, 4L_RS, 8L_RS, and 16L_RS for both RW and RW+SW cases. Furthermore, the difference in duration to attain maximum cumulative net infiltration between RW and RW+SW increases as the number of laminae increases when BS is the topmost lamina. In contrast, for profiles with RS as the topmost lamina, this difference in duration decreases with the increase in laminae. A similar trend in the difference of days to slope failure can be observed from Table 3, where when BS constitutes the topmost lamina, the difference in days to failure increases with the number of laminae, whereas a reverse trend of decreasing difference in days of slope failure is observed for laminae arrangements with RS as the topmost lamina. This observation further strengthens the link between FoS and infiltration in the respective soil slope profiles. From Table 3 and Table 5, it can also be stated that slope failure occurs in all the soil slope profiles sufficiently before maximum cumulative net infiltration is achieved in the sloping soil profiles.

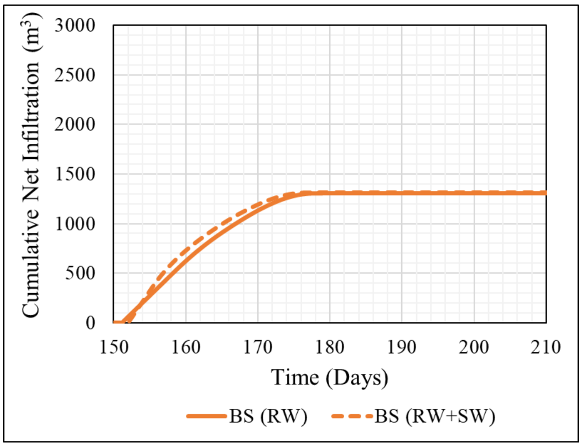
Cumulative Net Infiltration (m^3)
Time (Days)
BS (RW)
BS (RW+SW)

(a)

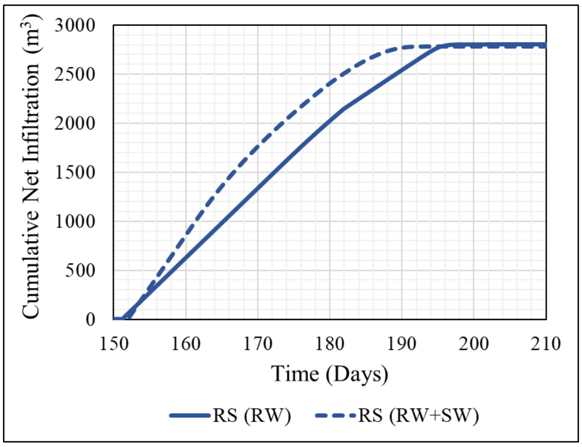
Cumulative Net Infiltration (m^3)
Time (Days)
RS (RW)
RS (RW+SW)

(b)

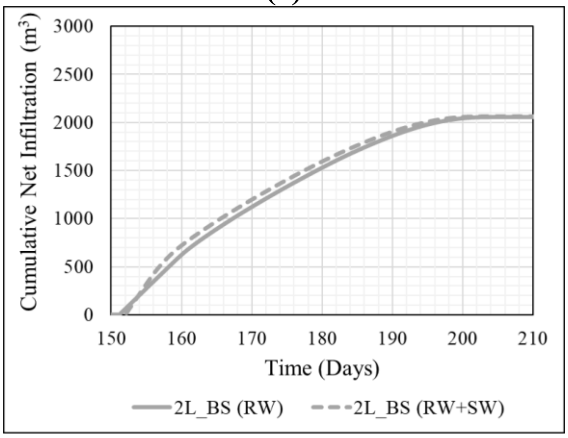
Cumulative Net Infiltration (m^3)
Time (Days)
2L_BS (RW)
2L_BS (RW+SW)

(c)

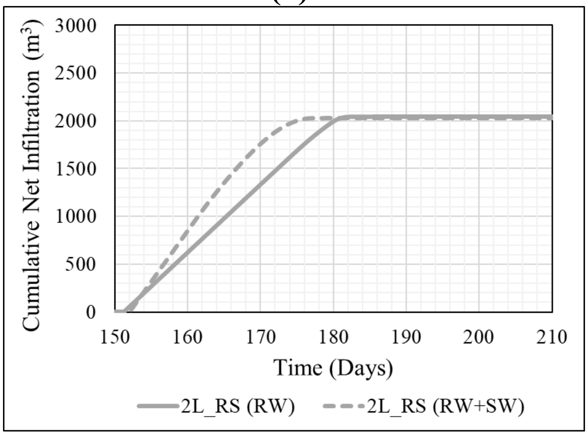
Cumulative Net Infiltration (m^3)
Time (Days)
2L_RS (RW)
2L_RS (RW+SW)

(d)

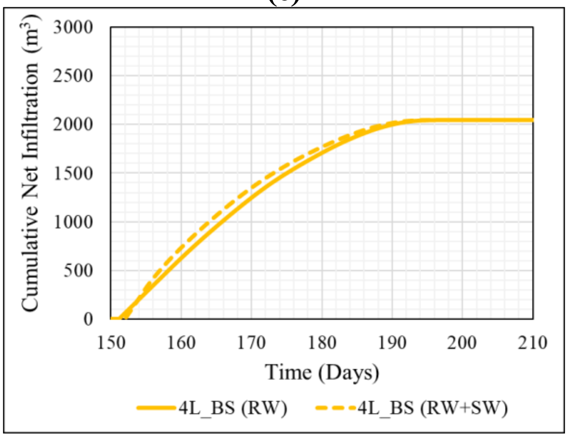
Cumulative Net Infiltration (m^3)
Time (Days)
4L_BS (RW)
4L_BS (RW+SW)

(e)

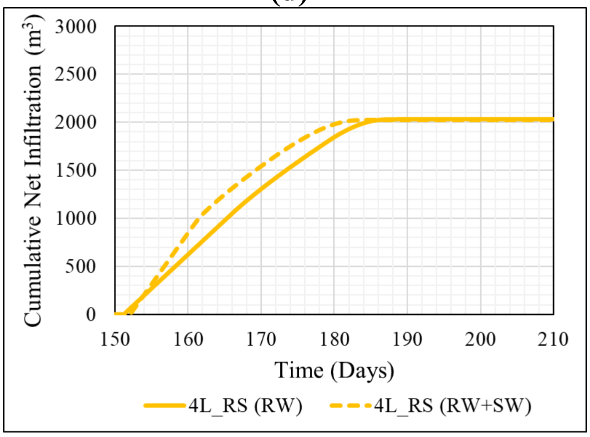
Cumulative Net Infiltration (m^3)
Time (Days)
4L_RS (RW)
4L_RS (RW+SW)

(f)

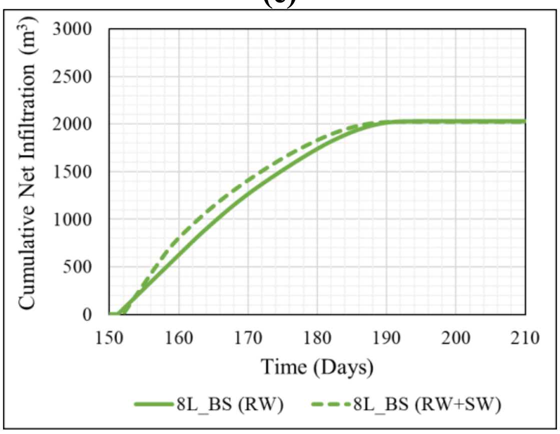
Cumulative Net Infiltration (m^3)
Time (Days)
8L_BS (RW)
8L_BS (RW+SW)

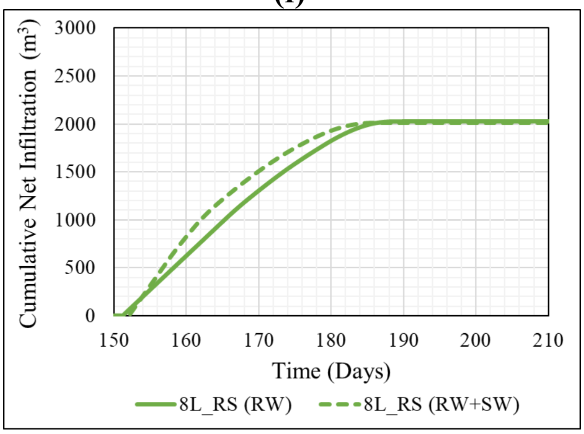
Cumulative Net Infiltration (m^3)
Time (Days)
8L_RS (RW)
8L_RS (RW+SW)

(g) (h)

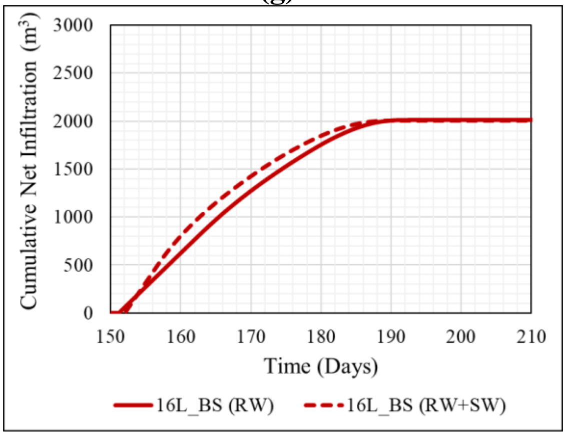

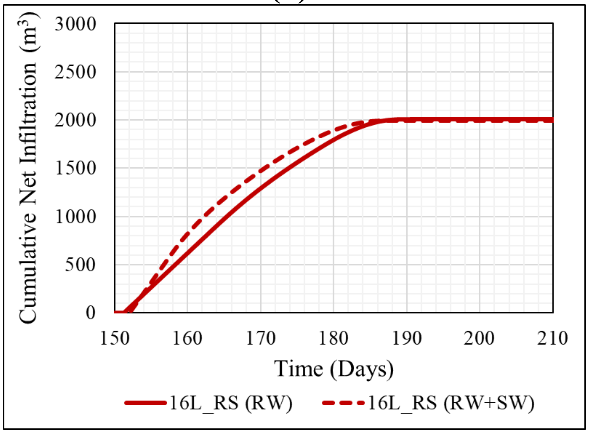

(i) (j)

Figure 7. Variation in cumulative net infiltration in slope profiles for RW and RW+SW scenarios (a) BS (b) RS (c) 2L_BS (d) 2L_RS (e) 4L_BS (f) 4L_RS (g) 8L_BS (h) 8L_RS (i) 16L_BS (j) 16L_RS

From Table 4, it is observed that the maximum cumulative net infiltration at the end of the study period decreases as the number of laminae increases for both types of sequential arrangements. However, the reconstituted varved clay slope profiles with BS as the topmost lamina show higher magnitudes of cumulative net infiltration compared to slope profiles with RS as the topmost lamina. The last column of Table 4 shows the differences in magnitudes of cumulative net infiltration between the two sequential arrangements corresponding to the same number of laminae. It can be observed that as the numbers of layer increases, the difference in magnitudes of the cumulative net infiltration between the two types of varved sequential arrangements decreases.

In the slopes with reconstituted varved clay profiles, the delayed slope failure when BS is the topmost lamina (Section 3.1), along with the delayed attainment and higher cumulative net infiltration by the end of the study compared to when RS is the topmost lamina, is attributed to the barrier and breakthrough phenomenon. The barrier effect is commonly observed in layered soils when water infiltrates from a finer soil layer to a coarser soil layer under unsaturated conditions, such that the initial suction is greater than the breakthrough suction of both soils (as in the present case). Under such conditions, the infiltrating water from the finer layer is restricted from moving into the coarser layer due to the contrast in hydraulic properties between the two soils. The breakthrough suction, also known as the water-entry suction value, occurs when the matric suction at the interface between the fine-grained soil layer and coarse-grained soil gets lower than the water-entry suction value of the coarse-grained soil (Li et al., 2021). This suction is achieved by raising the water content in the fine-grained soil near the interface. The coarser the underlying soil, the greater the pressure head required for breakthrough to occur (Baker and Hillel, 1990). In this study, the geotechnical properties of BS and RS are such that BS is finer than RS (Table 2). Figure 3(b) shows the HCF curves for RS and BS, with the intersection of the HCF curves representing the breakthrough suction when BS overlies RS. For 2L_BS, 4L_BS, 8L_BS, and 16L_BS, breakthrough occurs 1, 2, 4, and 8 times, respectively, whereas for 2L_RS, 4L_RS, 8L_RS, and 16L_RS, breakthrough occurs 0, 1, 3, and 7 times, respectively. Therefore, fewer breakthroughs are observed when RS occupies the topmost layer in the laminae soil profiles. Therefore, the higher number of breakthrough events in reconstituted varved slopes with BS as the topmost lamina leads to delayed slope failure, as well as delayed attainment and higher cumulative net infiltration by the end of the study, compared to slopes with RS as the topmost lamina.

Table 4. Cumulative Net Infiltration at the end of study period in different slope profiles

Soils	**No. of Laminae in slope profile**	**Cumulative Net Infiltration (m^3)**		**Difference (m^3)**
		Reconstituted Varved Clay with BS as topmost lamina	**Reconstituted Varved Clay with RS as topmost lamina**	
Reconstituted Varved Clay slope profiles	2	2059.64	2035.85	23.79
	4	2043.52	2027.36	16.17
	8	2029.87	2018.77	11.10
	16	2009.91	2001.19	8.72
	Soils	**Cumulative Net Infiltration (m^3)**		
Homogenous soil slope profiles	RS	2793.28		
	BS	1309.91		

Table 5. Time (in Days) when Maximum Cumulative Net Infiltration is achieved

Soils	**Slope Profiles**	**RW**	**RW+SW**	**RW-(RW+SW)**
Homogenous	RS	204.0	193.6	10.4
	BS	179.6	178.0	1.6
Reconstituted Varved Clay with BS as topmost lamina	2L_BS	202.2	202.8	0.6
	4L_BS	196.6	195.4	1.2
	8L_BS	194.0	191.6	2.4
	16L_BS	192.8	190.2	2.6
Reconstituted Varved Clay with RS as topmost lamina	2L_RS	185.6	179.2	6.4
	4L_RS	188.8	184.4	4.4
	8L_RS	190.0	186.4	3.6
	16L_RS	190.8	187.4	3.4

Figures 8(a) to 8(j) present graphical plots of cumulative runoff with time for all soil profiles considered in this study. The runoff for different soil profiles begins at different times during the summer season. The graphs clearly depict a notable increase in runoff in case of RW+SW as compared to RW. Furthermore, it is observed that the homogeneous BS slope profile exhibits the highest cumulative runoff, while the homogeneous RS slope profile displays the lowest cumulative runoff among all the considered soil slope profiles at the end of the study period. The magnitude of cumulative runoff at the end of the study period is listed in Table 6. It is observed from the table that the cumulative runoff at the end of the study period is slightly higher in the case of laminae profiles with RS constituting the topmost lamina as compared to the laminae profiles with BS as the topmost lamina. These runoff trends show an inverse relationship with infiltration. Cumulative net infiltration is greater when BS is the topmost lamina but decreases as the number of laminae increases, while runoff increases. More infiltration leads to less runoff, and vice versa. Additionally, the difference in cumulative runoff between RS and BS decreases as the number of laminae increases, corresponding to the trend observed in net infiltration.

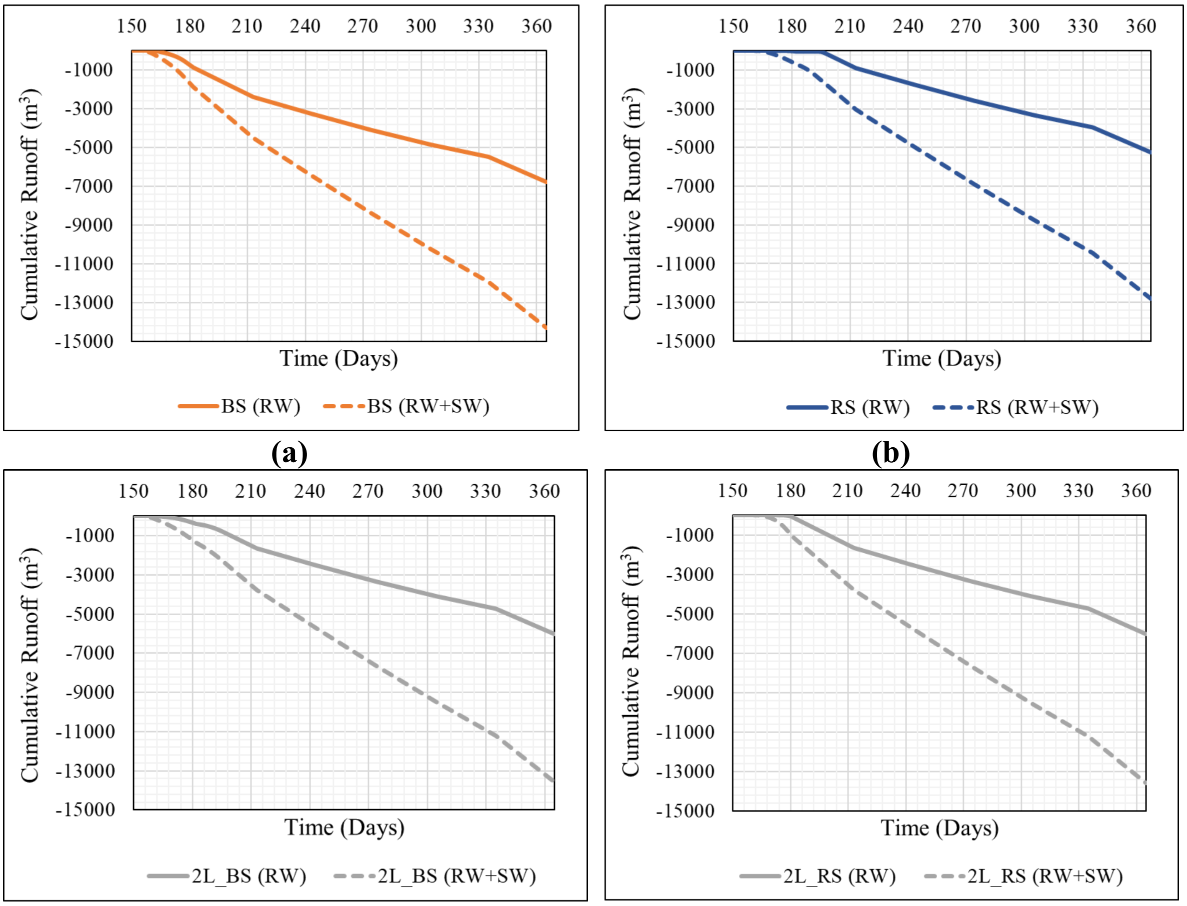

(a) **(b)**

(c) **(d)**

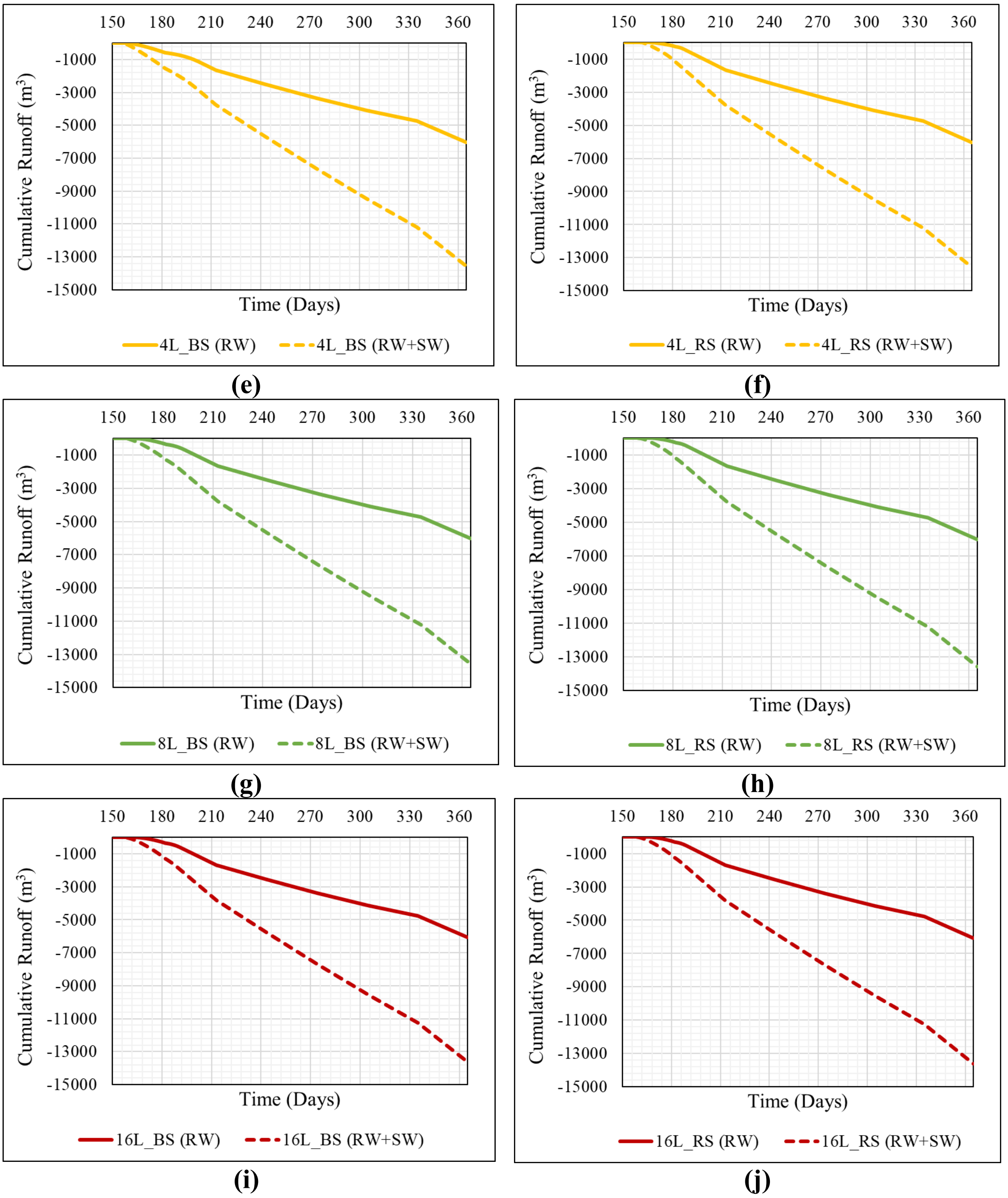

Figure 8. Variation in cumulative runoff in slope profiles for RW and RW+SW scenarios (a) BS (b) RS (c) 2L_BS (d) 2L_RS (e) 4L_BS (f) 4L_RS (g) 8L_BS (h) 8L_RS (i) 16L_BS (j) 16L_RS

Table 7 shows the duration (in days) at which runoff begins in the different slope profiles considered in this study. For all slope profiles, runoff begins much earlier in the case of RW+SW compared to RW. It is further observed that when BS occupies the topmost lamina, the time when runoff starts is delayed as the number of laminae increases. Conversely, for the slope profile with RS as the topmost lamina, the runoff begins earlier with an increased number of laminae for both RW and RW+SW cases. In reconstituted varved clay soil profiles with BS constituting the topmost soil, it is observed that for RW+SW consideration, runoff initiation is the same for BS, 2L_BS, and 4L_BS soil profiles. This indicates that, for higher exposure to water, runoff initiation is primarily influenced by the properties of the topmost lamina. Furthermore, the difference in days for runoff initiation between RW and RW+SW generally increases with the increase in the number of laminae for the varved clay profiles with BS as the topmost lamina. In contrast, for other case of sequential arrangement of laminae in sloping soil, this difference decreases with the increase in laminae.

Table 6. Cumulative runoff at the end of study period for different slope profiles

Soils	**No. of Laminae in slope profile**	**Cumulative Runoff (m^3)**		**Difference (m^3)**
		Reconstituted Varved Clay with BS as topmost lamina	**Reconstituted Varved Clay with RS as topmost lamina**	
Reconstituted Varved Clay slope profiles	2	9785.35	9798.54	13.19
	4	9798.60	9809.70	11.11
	8	9810.88	9819.44	8.55
	16	9830.16	9837.57	7.41
	Soils	**Cumulative Runoff (m^3)**		
Homogenous soil slope profiles	RS	9031.05		
	BS	10542.90		

Table 7. Number of days required to initiate runoff

Soils	**Slope Profiles**	**RW**	**RW+SW**	**RW-(RW+SW)**
Homogenous	RS	170.2	160.0	10.2
	BS	157.8	155.0	2.8
Reconstituted Varved Clay with BS as topmost lamina	2L_BS	157.2	155.0	2.2
	4L_BS	157.8	155.0	2.8
	8L_BS	160.8	155.2	5.6
	16L_BS	161.0	156.0	5.0
Reconstituted Varved Clay with RS as topmost lamina	2L_RS	170.6	160.0	10.6
	4L_RS	166.4	159.8	6.6
	8L_RS	163.8	157.4	6.4
	16L_RS	162.4	157.0	5.4

3.3 Temporal Dynamics of Pore-Water Pressure in Different Soil Profiles

Figures 9 and 10 illustrate the temporal variation of pore-water pressure in homogeneous BS and layered 2L_BS slope profiles. Although such pore-water pressure contours at different time steps are generated for all soil profiles under both RW and RW+SW conditions, only the homogeneous BS and 2L_BS slope profiles under RW conditions are shown here for illustrative purposes. Figures 9(a-c) and 10(a-c) represent pore-water pressure conditions prior to failure in the corresponding RS and 2L_BS slope profiles, respectively. Figure 9(c) and 10(c) portray the pore-water pressure distribution just before FoS drops below 1 for BS and 2L_BS slope profiles, respectively, which happens at the 171^{th} and 186.8^{th} day respectively. Further, Figures 9(d) and 10(d) present pore-water pressure distributions at the onset of slope failure that happens at the 171.2^{th} day and 187^{th} day for the RS and 2L_BS slope profiles, respectively. Finally, Figures 9(e-f) and 10(e-f) depict the pore-water pressure distribution in the post-failure scenario of BS and 2L_BS slopes, respectively.

Both Figures 9 and 10 illustrate that the toe of the slope loses suction and migrates to suction earlier than the other areas, as indicated by pore-water pressures being equal to or exceeding 0 kPa (represented by the red-shaded contour). In the 2L_BS profile, the lower lamina saturates first distinctively (Figure 10c) because of the differential permeability in the laminae. However, the slope failure initiates only when the saturation extends to the upper lamina and slope surface, as shown in Figure 6d. For both the cases, as time elapses, the extent of saturation in the slope keeps on expanding, which corresponds to a continuous decrease in the FoS, as illustrated in Figure 5 (FoS vs. Time). Once the slope becomes fully saturated, the FoS reaches its minimum value and remains constant for the portion of the terrain analyzed for stability. These temporal images confirm an increase in pore-water content in the sloping terrain, which is consistent with the rise in cumulative net infiltration over time, as illustrated in Figure 7. The net cumulative infiltration becomes constant after certain duration once the terrain is fully saturated.

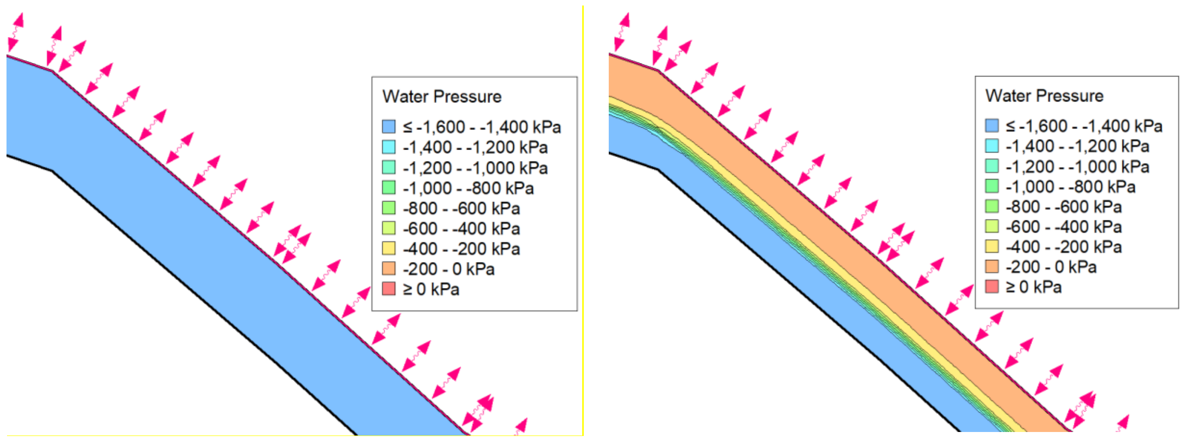

(a) (b)

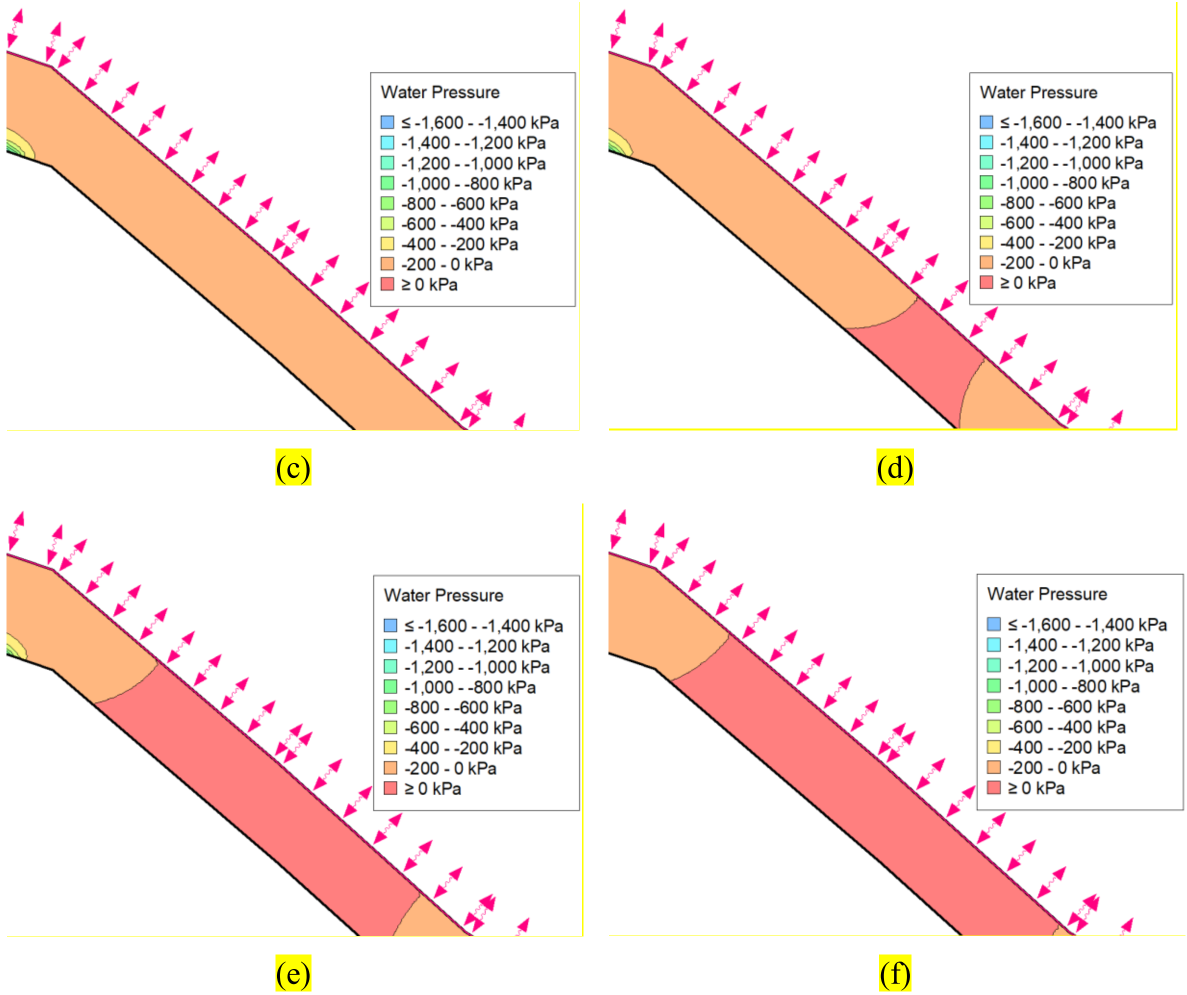

Figure 9. Temporal variation in pore-water pressure under rainwater infiltration for the homogeneous BS slope profile across different days: (a) Day 151, (b) Day 161, (c) Day 171, (d) Day 171.2, (e) Day 171.4, and (f) Day 172.4

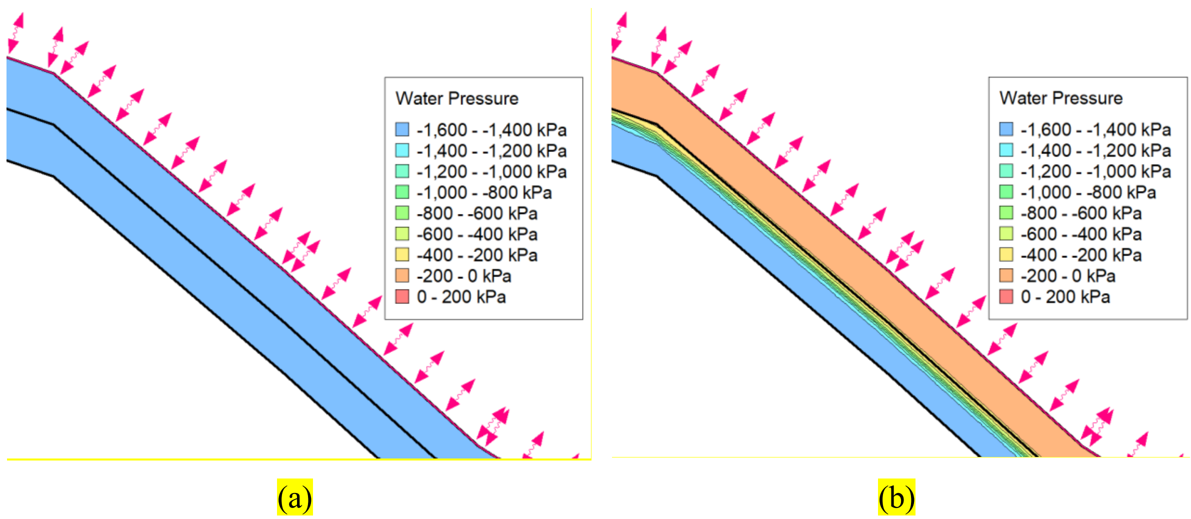

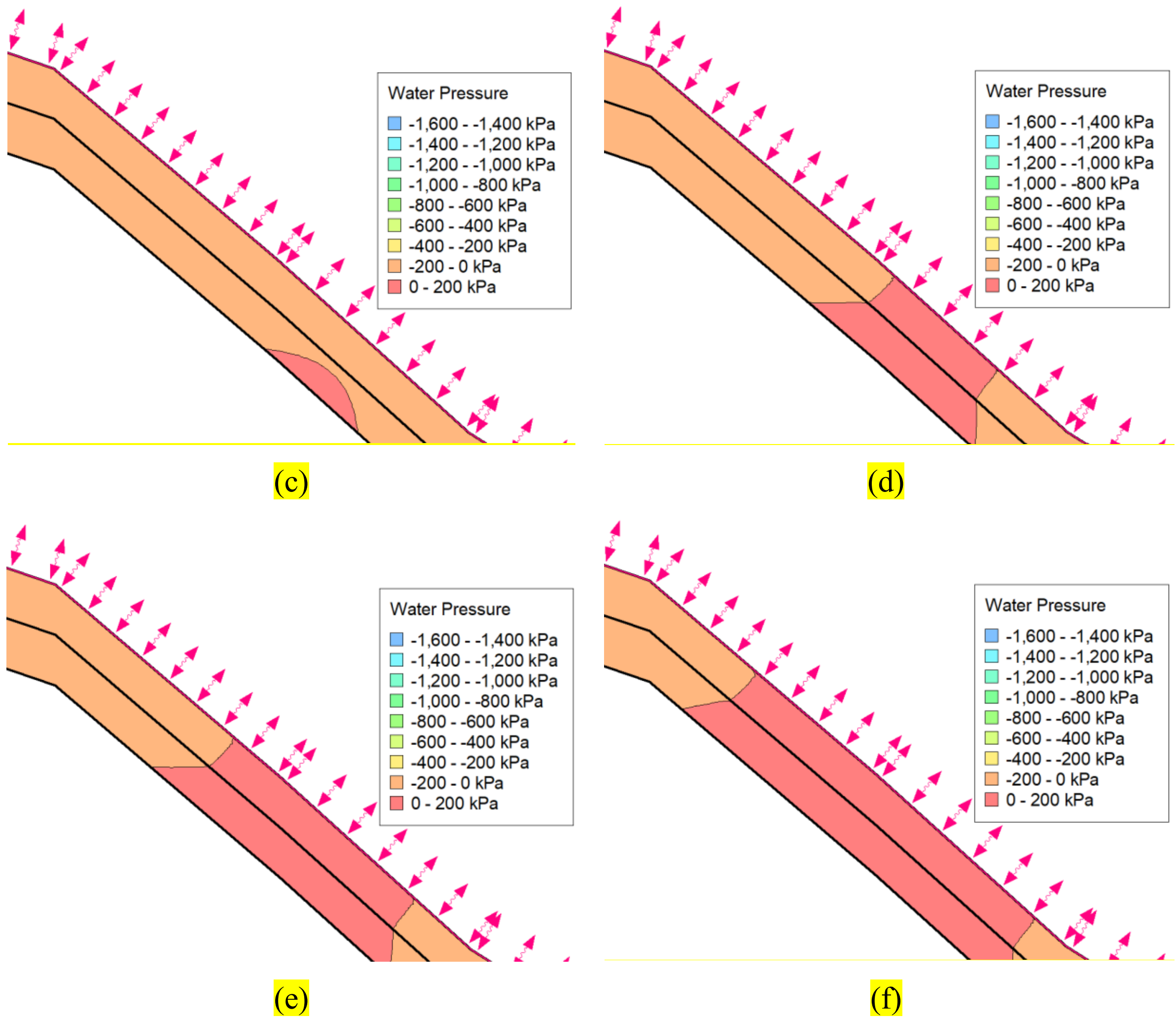

Figure 10. Temporal variation in pore-water pressure under rainwater infiltration for the 2L_BS reconstituted varved clay slope profile across different days: (a) Day 151 (b) Day 161 (c) Day 186.8 (d) Day 187 (e) Day 187.2 and (f) 188.2

4. Conclusions

In the present study, the effects of water infiltration from two climatic scenarios (RW and RW+SW) on homogeneous profiles (RS and BS) and reconstituted varved clay profiles (2-Layered, 4-Layered, 8-Layered and 16-Layered) with two different sequential arrangements, are investigated. The analysis focuses on slope stability, the area of soil mass affected by failure, cumulative net infiltration, and cumulative runoff in various soil slope profiles. The key findings and conclusions drawn from the study are summarized below:

- Early slope failure, earlier attainment of maximum cumulative net infiltration, and earlier runoff are observed under RW+SW climatic conditions compared to RW alone. The RW+SW scenario also results in higher runoff volume due to the additional water from snowmelt combined with rainwater.

- In reconstituted varved clay slope profiles, the laminae structure leads to a transitional mode of failure, while homogeneous slope profiles exhibit a circular slip surface at failure.
- The arrangement of RS and BS, along with the number of laminae in reconstituted varved clay profiles, significantly impacts the time at which slope fails, the area of soil mass involved in failure, cumulative net infiltration, cumulative runoff, and the timing of these events. In slope profiles where BS is the topmost lamina, the critical slip surface forms at shallower depths, with its depth depending on the number of laminae. In profiles where RS is the topmost lamina, the critical slip surface penetrates the full 4 m depth. This results in a smaller area of soil mass involved in failure when BS is the topmost lamina, compared to when RS is the topmost lamina. Additionally, as the number of laminae increases, the affected area due to slope failure increases in both sequential arrangements.
- Reconstituted varved clay slope profiles with RS as the topmost lamina fail earlier and achieve maximum cumulative net infiltration before those with BS as the topmost lamina. This is due to the lesser number of BS-RS interface in profiles with RS as the topmost lamina, which results in fewer occurrences of the barrier and breakthrough effect compared to profiles with BS as the topmost lamina. Additionally, the time to reach maximum cumulative net infiltration is uniquely linked to the timing of slope failure for each profile. The longer it takes for a profile to attain maximum infiltration, the later the slope failure occurs.
- Homogeneous BS slope profiles exhibit the highest cumulative runoff, while RS slope profiles show the lowest cumulative runoff among all the slope profiles at the end of the study period. Conversely, the cumulative net infiltration is highest for RS slope profiles and lowest for BS slope profiles. The reconstituted varved clay profiles exhibit intermediate magnitudes of both cumulative runoff and cumulative net infiltration, lying between the corresponding magnitudes of RS and BS. While the cumulative runoff increases with the number of laminae in reconstituted varved clay slopes, the cumulative net infiltration decreases with the increase in the number of laminae in the varved slopes.

In conclusion, the present study highlights the complex interactions among soil composition, the sequential arrangement of laminae, slope stability, infiltration, and runoff under varying water flux scenarios and different climatic conditions. This research is particularly relevant to glaciated regions, where rapid snowmelt due to climate change significantly alters the hydrological dynamics of the region. These altered dynamics lead to increased water volumes that contribute to both infiltration and runoff, which have the potential to trigger early slope instabilities. The study specifically emphasizes the effects of laminae arrangement and the number of laminae in varved deposits in glacial regions on the induced slope stability and hydrological behavior. The findings underscore the need to incorporate detailed laminae composition in slope stability assessments and water balance studies in such glacial environments. Such an understanding is crucial for effective water management and predicting the occurrence of landslides in these regions.

5. Limitations of the Present Study

Despite the detailed analysis of stability and water balance in different soil slope profiles, this study has certain limitations. A deterministic approach has been adopted which utilizes constant magnitude for geotechnical, hydrological and geometrical properties. However, in natural conditions, these properties exhibit spatial variability, which can significantly influence slope stability and hydrological dynamics, including infiltration and runoff. While these simplifications were necessary to ensure computational feasibility and maintain focus on the primary objectives, future research could incorporate probabilistic modeling approaches. Such approaches would account for randomness and uncertainty, enhancing the robustness and applicability of slope stability assessments and water balance studies. Further, this particular study analyses the glaciatic slope stabilities based on a limit-equilibrium framework. It is to be noted that a comprehensive finite element based stability of slopes comprising multi-layered stratification would provide more nuanced results subjected to hydrological processes. A coupled stress-deformation based multi-layered slope stability would provide more insightful results while emphasizing the influence of constitutive mechanics of the participating materials as well as their interface interactions.

References

Ahmad, N., Hashimi, N. (1974). Glacial History of Kolahoi Glacier, Kashmir, India. Journal of Glaciology 13(68), 279-283. http://doi.org/10.3189/S002214300002308X

Anderson, R.Y., Dean, W.E. (1988). Lacustrine varve formation through time. Palaeogeography, Palaeoclimatology, Palaeoecology 64(1-4), 215-235. https://doi.org/10.1016/0031-0182(88)90055-7

ASTM. 2002. Standard test method for determination of the soil water characteristic curve for desorption using a hanging column, pressure extractor, chilled mirror hygrometer, and/or centriguge, D 6836-02, American Society of Testing Materials. D6836 Method D.

ASTM. 2015. Standard test method for measurement of hydraulic conductivity of porous material using a rigid-wall, compaction-mold permeameter. D5856−15.

ASTM. 2011. Standard test method for direct shear test of soils under consolidated drained conditions. ASTM D3080/D3080M. West Conshohocken, PA: ASTM.

Baker, R. S., and Hillel, D. (1990). Laboratory tests of a theory of fingering during infiltration into layered soils. Soil Science Society of America Journal 54(1), 20-30. https://doi.org/10.2136/sssaj1990.03615995005400010004x

Beukema, S., Krishnamurthy, R., Juyal, N., Basavaiah, N., Singhvi, A. (2011). Monsoon variability and chemical weathering during the late Pleistocene in the Goriganga basin, higher central Himalaya, India. Quaternary Research 75(3), 597-604. https://doi.org/10.1016/j.yqres.2010.12.016

Bhasin, R., Aslan, G., Dehls, J. (2023). Ground investigations and detection and monitoring of landslides using SAR interferometry in Gangtok, Sikkim Himalaya. GeoHazards 4(1), 25-39. https://doi.org/10.3390/geohazards4010003

Bhattacharyya, A., Ranhotra, P.S., Gergan, J.T. (2011). Vegetation vis-à-vis climate and glacier history during 12,400 to 5,400 yr BP from Dokriani valley, Garhwal Himalaya, India. Journal of Geological Society of India 77, 401–408. https://doi.org/10.1007/s12594-011-0047-y

Burakov, D.A., Ivanova, O.I. (2010). Analysis of formation and forecast of spring snowmelt flood runoff in forest and forest-steppe basins of Siberian rivers. Russian Meteorology and Hydrology 35, 421–431. https://doi.org/10.3103/S1068373910060099

Carey, M. (2005). Living and dying with glaciers: people's historical vulnerability to avalanches and outburst floods in Peru. Global and Planetary Change 47(2), 122-134. https://doi.org/10.1016/j.gloplacha.2004.10.007

Chatterjee, D., Murali Krishna, A. (2021). Stability analysis of two-layered non-homogeneous slopes. International Journal of Geotechnical Engineering 15(5), 617–623. https://doi.org/10.1080/19386362.2018.1465686

Chauniyal, DD., Semwal, S. (2021). A geomorphological interpretation of rishi ganga flash flood, Garhwal Himalaya, India. Journal of Indian Geomorphology 9, 89-103.

Dai, G., Zhang, F., Wang, Y. (2022). Stability analysis of layered slopes in unsaturated soils. Frontiers of Structural and Civil Engineering 16, 378–387. https://doi.org/10.1007/s11709-022-0808-2

Damiano, E., Greco, R., Guida, A., Oliveres, L., Picarelli, L. (2017). Investigation on rainwater infiltration into layered shallow covers in pyroclastic soils and its effect on slope stability. Engineering Geology 220, 208-218. https://doi.org/10.1016/j.enggeo.2017.02.006

Davenport, F.V., Herrera-Estrada, J.E., Burke, M., Diffenbaugh, N.S. (2019). Flood size increases nonlinearly across the western United States in response to lower snow-precipitation ratios. Water Resources Research 56(1), e2019WR025571. https://doi.org/10.1029/2019WR025571

de Vries, MVW., Ito, E., Shapley, M., Brignone, G., Romero, M., Wickert, A.D., Miller, L.H., MacGregor, K.R. (2022). Physical limnology and sediment dynamics of Lago Argentino, the world's largest ice-contact lake. Journal of Geophysical Research: Earth Surface 127(3). https://doi.org/10.1029/2022JF006598

Decagon Devices. WP4 dewpoint potentiometer – Operator's manual. Version 1.3. Pullman: Decagon Devices, Inc.; 2000.

Deng, Dp., Li, L., Zhao, Lh. (2019). Stability analysis of a layered slope with failure mechanism of a composite slip surface. International Journal of Geomechanics ASCE 19(6). https://doi.org/10.1061/(ASCE)GM.1943-5622.0001417

Dijkstra, T., Dixon, N. (2010). Climate change and slope stability in the UK: challenges and approaches. Quarterly Journal of Engineering Geology and Hydrogeology 43(4), 371–385. https://doi.org/10.1144/1470-9236/09.036

Dikshit, A., Sarkar, R., Pradhan, B., Segoni, S., Alamri, A.M. (2020). Rainfall induced landslide studies in Indian Himalayan Region: A critical review. Applied Sciences 10(7), 2466. https://doi.org/10.3390/app10072466

Dongli, S., Dongdong, L., Yingying, Yi, L., Cuilan, X., Xin, Q., Fang, C. (2014). Profile characteristics of temporal stability of soil water storage in two land uses. Arabian Journal of Geosciences 7, 21–34. https://doi.org/10.1007/s12517-013-0838-0\

Eden, W.J. (1955). Laboratory study of varved clay from Steep Rock Lake, Ontario. American Journal of Science 253, 659-674. https://doi.org/10.4224/20331506

Eigenbrod, K.D., Burak, J.B. (1991). Effective stress paths and pore-pressure responses during undrained shear along the bedding planes of varved Fort William Clay. Canadian Geotechnical Journal 28 (6), 804-811. https://doi.org/10.1139/t91-097

Flieger-Szymanska, M., Machowiak, K., Krawczyk, D., Wanatowski, D. (2019). Characterisation of mineral composition and strength parameters of varved clays. In: Proceedings of the 17th European Conference on Soil Mechanics and Geotechnical Engineering (ECSMGE 2019). XVII ECSMGE 2019, 01-06 Sep 2019, Reykjavik, Iceland. International Society for Soil Mechanics and Geotechnical Engineering. ISBN 978-9935-9436-1-3

Florkiewicz, A., Flieger-Szymanska, M., Machowiak, K., Wanatowski, D. (2014). Engineering properties of varved clays from the Junikowski Stream Valley in Poland. Conference: Proc. 4th International Conference on Geotechnical Engineering for Disaster Mitigation and Rehabilitation (4th GEDMAR) At: Kyoto, Japan Volume: Geotechnics for Catastrophic Flooding Events

Fredlund, D.G., Krahn, J. (1977). Comparison of slope stability methods of analysis. Canadian Geotechnical Journal 14, 429-439. https://doi.org/10.1139/t77-045

Fredlund, D.G., Morgenstern, N.R., Widger, R.A. (1978). Shear strength of unsaturated soils. Canadian Geotechnical Journal 15(3), 313–321. https://doi.org/10.1139/t78-029

Hall, D.K., Martinec, J. (1985). Remote sensing of ice and snow. Remote Sensing Applications (RSA), Dordrecht: Springer Netherlands. ISBN 978-94-009-4842-6.

IPCC, 2014: Climate Change 2014: Synthesis report. Contribution of working groups I, II and III to the fifth assessment report of the intergovernmental panel on climate change [Core Writing Team, R.K. Pachauri and L.A. Meyer (eds.)]. IPCC, Geneva, Switzerland, 151 pp.

IS:14243 (Part-2)-1995. Selection and Development of Site for Building in Hill Areas-Guidelines. Bureau of Indian Standards, New Delhi, India.

IS:2720 (Part 3/Sec-2)-1980. Methods of test for soils: Determination of specific gravity - Part 3/Section 2: Fine, medium, and coarse-grained soils. Bureau of Indian Standards, New Delhi, India.

IS:2720 (Part 4)-1980. Methods of test for soils: Grain size analysis. Bureau of Indian Standards, New Delhi, India.

IS:2720 (Part 5)-1985. Methods of test for soils: Determination of liquid limit and plastic limit. Bureau of Indian Standards, New Delhi, India.

IS:2720 (Part 7)-1980. Methods of test for soils: Determination of water content-dry density relation using light compaction. Bureau of Indian Standards, New Delhi, India.

Juyal, N., Pant, R.K., Basavaiah, N., Bhushan, Jain, M., Saini, N.K., Yadava, M.G., Singhvi, A.K. (2009). Reconstruction of Last Glacial to early Holocene monsoon variability from relict lake sediments of the Higher Central Himalaya, Uttarakhand, India. Journal of Asian Earth Sciences 34(3), 437-449. https://doi.org/10.1016/j.jseaes.2008.07.007

Kansal, M.L., Singh, S. (2022). Flood management issues in hilly regions of Uttarakhand (India) under changing climatic conditions. Water 14(12), 1879. https://doi.org/10.3390/w14121879.

Kazi, A. (1967). Aspects of the engineering geology of laminated glacial lake clays. Thesis, Imperial College of Science London.

Krawczyk, D., Szymanska, M.F. (2018). The value of plasticity index (IP) and liquidity index (IL) of North Polish ablation boulder clays and varved clays depending of the method of its determination. Scientific Review – Engineering and Environmental Sciences 27 (2), 167–174. https://doi.org/10.22630/PNIKS.2018.27.2.16

Kropáček, J., Vilímek, V., Mehrishi, P. A. (2021). Preliminary assessment of the Chamoli rock and ice avalanche in the Indian Himalayas by remote sensing. Landslides 18(4), 3489–3497. https://doi.org/10.1007/s10346-021-01742-1

Lagmay, A.M.F.A., Escape, C., Ybañez, A.A., Suarez, J.K., Cuaresma, G. (2020). Anatomy of the Naga City landslide and comparison with historical debris avalanches and analog models. Frontiers in Earth Science 8, 312. http://doi.org/10.3389/feart.2020.00312

Li, Y., Satyanaga, A., and Rahardjo, H. (2021). Characteristics of unsaturated soil slope covered with capillary barrier system and deep-rooted grass under different rainfall patterns. International Soil and Water Conservation Research 9(3), 405-418. https://doi.org/10.1016/j.iswcr.2021.03.004

Liu, L., Sletten, R.S., Hagedorn, B., Hallet, B., McKay, C.P., Stone, J.O. (2015). An enhanced model of the contemporary and long-term (200 ka) sublimation of the massive subsurface ice in Beacon Valley, Antarctica. Journal of Geophysical Research: Earth Surface 120(8), 1596-1610. https://doi.org/10.1002/2014JF003415

Luo, Z., Fan, J., Shao, M., Hu, W., Yang, Q., Zhang, S. (2023). Soil water dynamics and groundwater evolutions of check dams under natural rainfall reduction in semi-arid areas. Journal of Hydrology 617, Part C, 129099. https://doi.org/10.1016/j.jhydrol.2023.129099

Lydzba, D., Tankiewicz, M. (2012). Preliminary study of failure anisotropy characterization of varved clay. AGH Journal of Mining and Geoengineering 36 (2), 229-234.

Martha, T.R., Roy, P., Jain, N., Kumar, K.V., Reddy, P.S., Nalini, J., Sharma, S.V.S.P., Shukla, A.K., Rao, K.H.V.D., Narendra, B., Rao, P.V.N., Muralikrishnan, S. (2021). Rock avalanche induced flash flood on 07 February 2021 in Uttarakhand, India—a photogeological reconstruction of the event. Landslides 18, 2881–2893. https://doi.org/10.1007/s10346-021-01691-9

Martha, T.R., Roy, P., Raj K, B.G., Kumar, K.V. (2013). Landslides due to extreme events -An assessment of June, 2013 Uttarakhand (India) disaster using high resolution satellite data. Conference: Joint International Workshop of ISPRS VIII/1 and WG IV/4 on Geospatial Data for Disaster and Risk Reduction, November 21-22, 2013.

Mei, Xm., Ma, L., Zhu, Qk., Wang, S., Zhang, D., Wang, Y. (2018). Responses of soil moisture to vegetation restoration type and slope length on the loess hillslope. Journal of Mountain Science 15, 548–562. https://doi.org/10.1007/s11629-017-4415-y

Mir, R.A., Jain, S.K., Lohani, A.K., Saraf, A.K. (2018). Glacier recession and glacial lake outburst flood studies in Zanskar basin, western Himalaya. Journal of Hydrology 564, 376-396. https://doi.org/10.1016/j.jhydrol.2018.05.031.

Mishra, A., Liu, S.C. (2014). Changes in precipitation pattern and risk of drought over India in the context of global warming. Journal of Geophysical Research: Atmospheres 119(13), 7833- 7841. https://doi.org/10.1002/2014JD021471

Morgenstern, N.R., Price, V.E. (1965). The Analysis of the Stability of General Slip Surfaces. Géotechnique 15, 79–93. http://doi.org/10.1680/geot.1965.15.1.79

Netto, R.G., Benner, J. S., Buatois, L.A., Uchman, A., Mangano, M.G., Ridge, J.C., Kazakauskas, Gaigalas, A. (2012). Glacial Environments. Chapter-11 of Developments in Sedimentology 64, 299-327. https://doi.org/10.1016/B978-0-444-53813-0.00011-3

Nunes, G. B., Portelinha, F.H.M., Futai, M.M., Yoo, C. (2022). Numerical study of the impact of climate conditions on stability of geocomposite and geogrid reinforced soil walls. Geotextiles and Geomembranes 50(4), 807-824. https://doi.org/10.1016/j.geotexmem.2022.04.004

Palmer, A.P., Bendle, J.M., MacLeod, A., Rose, J., Thorndycraft, V.R. (2019). The micromorphology of glaciolacustrine varve sediments and their use for reconstructing palaeoglaciological and palaeoenvironmental change. Quaternary Science Reviews, 226: 105964. https://doi.org/10.1016/j.quascirev.2019.105964

Pant, R. K., Juyal, N., Rautela, P., Yadav, M. G., Sangode, S. J. (1998). Climate instability during last glacial stage: Evidence from varve deposits at Goting, district Chamoli, Garhwal Himalaya, India. Current Science, 75(8): 850–855. http://www.jstor.org/stable/24101637

Rafiq, M., Rashid, I., Romshoo, S.A. (2016). Estimating land surface temperature and its lapse rate over Kashmir Valley using MODIS data. In Geostatistical and Geospatial Approaches for the Characterization of Natural Resources in the Environment, 723-728. New York, NY: Springer International Publishing.

Rafiq, M., Romshoo, S., Mishra, Jalal, F. (2019). Modelling Chorabari Lake outburst flood, Kedarnath, India. Journal of Mountain Science 16, 64–76. https://doi.org/10.1007/s11629-018-4972-8.

Rao, K.H.V.D., Rao, VV., Dadhwal, V.K., Diwakar, P.G. (2014). Kedarnath flash floods: A hydrological and hydraulic simulation study. Current Science 106(4), 598- 603. https://www.jstor.org/stable/24100068

Reddy, D.V. (2014). Landslides-debris flows floods earthquakes and tsunamis of Indian sub-continent- emergency preparedness plan – a typical analysis. 3rd World Conference on Applied Sciences, Engineering & Technology 27-29 September 2014, Kathmandu, Nepal.

Rist, A., Phillips, M. (2005). First results of investigations on hydrothermal processes within the active layer above alpine permafrost in steep terrain. Norsk Geografisk Tidsskrift - Norwegian Journal of Geography 59(2), 177-183. http://doi.org/10.1080/00291950510020574

Ruijsch, J., Verstegen, J.A., Sutanudjaja, E.H., Karssenberg, D. (2021). Systemic change in the Rhine-Meuse basin: Quantifying and explaining parameters trends in the PCR-GLOBWB global hydrological model. Advances in Water Resources 155, 104013. https://doi.org/10.1016/j.advwatres.2021.104013

Scaringi, G., Loche, M. (2022). A thermo-hydro-mechanical approach to soil slope stability under climate change. Geomorphology 401, 108108. https://doi.org/10.1016/j.geomorph.2022.108108

Seneviratne, S.I., N. Nicholls, D. Easterling, C.M. Goodess, S. Kanae, J. Kossin, Y. Luo, J. Marengo, K. McInnes, M. Rahimi, M. Reichstein, A. Sorteberg, C. Vera, and X. Zhang, 2012: Changes in climate extremes and their impacts on the natural physical environment. In: Managing the Risks of Extreme Events and Disasters to Advance Climate Change Adaptation [Field, C.B., V. Barros, T.F. Stocker, D. Qin, D.J. Dokken, K.L. Ebi, M.D. Mastrandrea, K.J. Mach, G.-K. Plattner, S.K. Allen, M. Tignor, and P.M. Midgley (eds.)]. A Special Report of Working Groups I and II of the Intergovernmental Panel on Climate Change (IPCC). Cambridge University Press, Cambridge, UK, and New York, NY, USA, pp. 109-230.

Shur, Y., Zhestkova, T. (2003). Cryogenic structure of a glacio-lacustrine deposit. Permafrost, Phillips, Springman & Arenson (eds), 1051-1056.

Singh, R., Singh, D., Gokani, S. A., Sreeush, M. G., Buchunde, P. S., Maurya, A. K., Singh, R. P., and Singh, A. K. (2015). Brief Communication: Climatic, meteorological and topographical causes of the 16–17 June 2013 Kedarnath (India) natural disaster event. Natural Hazards and Earth System Sciences 15, 1597–1601. https://doi.org/10.5194/nhess-15-1597-2015

Singh, S.P., Reshi, Z.A., Joshi, R. (2023). Treeline research in the Himalaya: Current understanding and future imperatives. In: Singh, S.P., Reshi, Z.A., Joshi, R. (eds) Ecology of Himalayan Treeline Ecotone. Springer, Singapore. https://doi.org/10.1007/978-981-19-4476-5_1.

Tang, A.M., Hughes, P.N., Dijkstra, T.A., Askarinejad, A., Brenčič, M., Cui, Y.J., Diez, J.J., Firgi, T., Gajewska, B., Gentile, F., Grossi, G., Jommi, C., Kehagia, F., Koda, E., ter Maat, H.W., Lenart, S., Lourenco, S., Oliveira M., Osinski, P., Springman, S.M., Stirling, R., Toll, D.G., Van Beek, V. (2018). Atmosphere–vegetation–soil interactions in a climate change context; impact of changing conditions on engineered transport infrastructure slopes in Europe. Quarterly Journal of Engineering Geology and Hydrogeology 51, 156-168. https://doi.org/10.1144/qjegh2017-103

Tankiewicz, M. (2016). Structure investigations of layered soil-varved clay. Annals of Warsaw University of Life Sciences-SGGW. Land Reclamation 48, 365 - 375. http://doi.org/10.1515/sggw-2016-0028

US Army Corps of Engineers. (1998). HEC-1 Flood Hydrograph Package. Hydrologic Engineering Center, (530) 756-1104. US Army Corps of Engineers, 609 Second Street, Davis, CA 95616.

van Genuchten, M. Th. A closed-form equation for predicting the hydraulic conductivity of unsaturated soils. Soil Science Society of American Journal 44, 892-898 (1980). https://doi.org/10.2136/sssaj1980.03615995004400050002x

Vanapalli, S.K., Fredlund, D.G., Pufahl, D.E., Clifton, A.W. (1996). Model for the prediction of shear strength with respect to soil suction. Canadian Geotechnical Journal 33, 379–392. http://doi.org/10.1139/t96-060

Vergnano, A., Oggeri, C., Godio, A. (2023). Geophysical–geotechnical methodology for assessing the spatial distribution of glacio-lacustrine sediments: The case history of Lake Seracchi. Earth Surface Processes and Landforms 48(7), 1374-1397. https://doi.org/10.1002/esp.5555

Wang, H., Yang, A., Jiang, S., Liu, N. (2023). Reconstruction of a Holocene landslide-dammed lake in the Yalong basin, Eastern Tibetan Plateau. Frontiers in Earth Science, 10. https://doi.org/10.3389/feart.2022.1042581

World Weather Online. Tawang Annual Weather Averages, Arunachal Pradesh, IN https://www.worldweatheronline.com/tawang-weather-averages/arunachal-pradesh/in.aspx

Worni, R., Stoffel, M., Huggel, C., Volz, C., Casteller, A., Luckman, B. (2012). Analysis and dynamic modeling of a moraine failure and glacier lake outburst flood at Ventisquero Negro, Patagonian Andes (Argentina). Journal of Hydrology 444, 134-145. https://doi.org/10.1016/j.jhydrol.2012.04.013

Ya, Y., Dongdong, L., Dongli, S. (2023). Simulating the effects of vegetation restoration and climate change on the long-term soil water balance on the Loess Plateau, 2021–2050. Journal of Hydrology 626 (Part A), 130260. https://doi.org/10.1016/j.jhydrol.2023.130260

Zou, Z.Y., Young, M.H., Li, Z., Wierenga, P.J. (2001). Estimation of depth averaged unsaturated soil hydraulic properties from infiltration experiments. Journal of Hydrology 242(1-2), 26-42. https://doi.org/10.1016/S0022-1694(00)00385-1